Since January 2020 Elsevier has created a COVID-19 resource centre with free information in English and Mandarin on the novel coronavirus COVID-19. The COVID-19 resource centre is hosted on Elsevier Connect, the company's public news and information website.

Cell Reports

Article

Parsing the role of NSP1 in SARS-CoV-2 infection

Graphical abstract

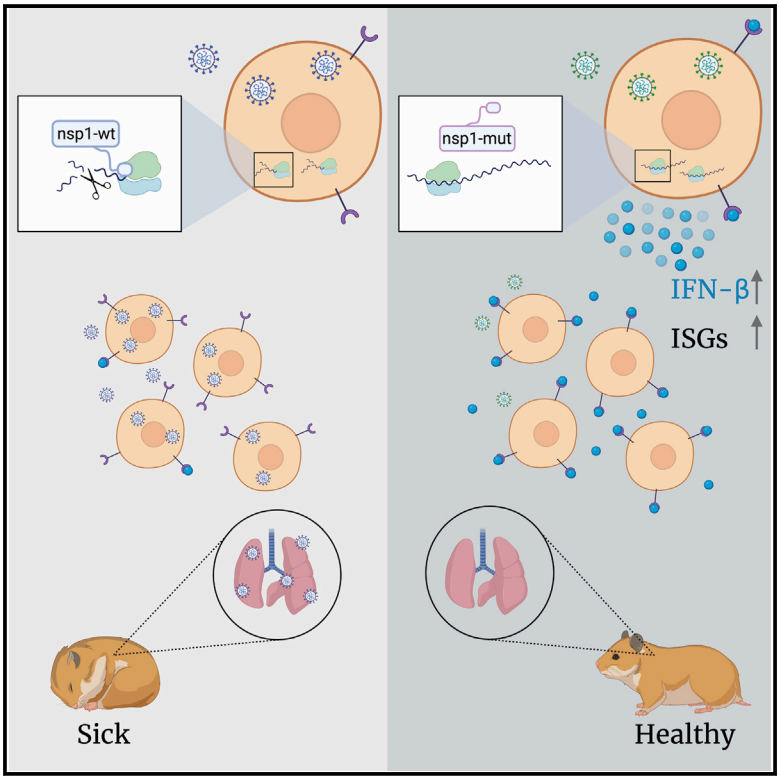

Highlights

- Nsp1 inhibits translation, induces mRNA degradation, and blocks nuclear mRNA export
- Nsp1 effects on translation, degradation, and export represent distinct functions
- Nsp1 is SARS-CoV-2 main shutoff factor, and it broadly targets translated cellular mRNAs
- Nsp1 functional importance lies explicitly in the attenuation of the interferon response

Authors

Tal Fisher, Avi Gluck, Krishna Narayanan, ..., Yoshihiro Kawaoka, Shinji Makino, Noam Stern-Ginossar

Correspondence

nirp@iibr.gov.il (N.P.), yoshihiro.kawaoka@wisc.edu (Y.K.), shmakino@utmb.edu (S.M.), noam.stern-ginossar@weizmann.ac.il (N.S.-G.)

In brief

Here, Fisher et al. show the importance of nsp1, a central shutoff factor in coronaviruses, during SARS-CoV-2 infection. nsp1 has broad activity, and it targets all translated cellular mRNA, but its functional importance in SARS-CoV-2 infection lies explicitly in blocking the IFN response.

Fisher et al., 2022, Cell Reports *39*, 110954
June 14, 2022
https://doi.org/10.1016/j.celrep.2022.110954

CellPress

Cell Reports

CellPress
OPEN ACCESS

Article

Parsing the role of NSP1 in SARS-CoV-2 infection

Tal Fisher,[1,8] Avi Gluck,[1,8] Krishna Narayanan,[2,8] Makoto Kuroda,[3,8] Aharon Nachshon,[1] Jason C. Hsu,[2] Peter J. Halfmann,[3] Yfat Yahalom-Ronen,[4] Hadas Tamir,[4] Yaara Finkel,[1] Michal Schwartz,[1] Shay Weiss,[4] Chien-Te K. Tseng,[2,5] Tomer Israely,[4] Nir Paran,[4,*] Yoshihiro Kawaoka,[3,6,7,*] Shinji Makino,[2,5,*] and Noam Stern-Ginossar[1,9,*]

[1]Department of Molecular Genetics, Weizmann Institute of Science, Rehovot 76100, Israel
[2]Department of Microbiology and Immunology, The University of Texas Medical Branch, Galveston, TX 77555-1019, USA
[3]Department of Pathobiological Sciences, School of Veterinary Medicine, University of Wisconsin, Madison, WI 53711, USA
[4]Department of Infectious Diseases, Israel Institute for Biological Research, Ness Ziona 74100, Israel
[5]Institute for Human Infections and Immunity, The University of Texas Medical Branch, Galveston, TX 77555-1019, USA
[6]Department of Virology, Institute of Medical Science, University of Tokyo, Tokyo 108-8639, Japan
[7]The Research Center for Global Viral Diseases, National Center for Global Health and Medicine Research Institute, Tokyo 162-8655, Japan
[8]These authors contributed equally
[9]Lead contact
*Correspondence: nirp@iibr.gov.il (N.P.), yoshihiro.kawaoka@wisc.edu (Y.K.), shmakino@utmb.edu (S.M.), noam.stern-ginossar@weizmann.ac.il (N.S.-G.)
https://doi.org/10.1016/j.celrep.2022.110954

SUMMARY

Severe acute respiratory syndrome coronavirus 2 (SARS-CoV-2) leads to shutoff of protein synthesis, and nsp1, a central shutoff factor in coronaviruses, inhibits cellular mRNA translation. However, the diverse molecular mechanisms employed by nsp1 as well as its functional importance are unresolved. By overexpressing various nsp1 mutants and generating a SARS-CoV-2 mutant, we show that nsp1, through inhibition of translation and induction of mRNA degradation, targets translated cellular mRNA and is the main driver of host shutoff during infection. The propagation of nsp1 mutant virus is inhibited exclusively in cells with intact interferon (IFN) pathway as well as *in vivo*, in hamsters, and this attenuation is associated with stronger induction of type I IFN response. Therefore, although nsp1's shutoff activity is broad, it plays an essential role, specifically in counteracting the IFN response. Overall, our results reveal the multifaceted approach nsp1 uses to shut off cellular protein synthesis and uncover nsp1's explicit role in blocking the IFN response.

INTRODUCTION

All viruses rely on the cellular ribosomes to translate their mRNAs into polypeptides. A common viral strategy to achieve this is to impair the translation of cellular mRNAs in a process termed "host shutoff." Host shutoff is thought to contribute to viral takeover in two main ways: it helps to redirect translational resources and specifically ribosomes toward viral mRNAs, and it blocks the ability of infected cells to mount an efficient antiviral response (Stern-Ginossar et al., 2019).

Viruses utilize diverse strategies to shutoff host protein synthesis, including interference in mRNA transcription, processing and export out of the nucleus, and induction of mRNA degradation, as well as direct inhibition of the translation machinery (Stern-Ginossar et al., 2019). Coronaviruses (CoVs) are known to cause host shutoff, and several strategies have been proposed for how CoVs interfere with host protein synthesis (Abernathy and Glaunsinger, 2015; Nakagawa and Makino, 2021; Nakagawa et al., 2016). We recently demonstrated that severe acute respiratory syndrome coronavirus 2 (SARS-CoV-2) infection leads to a reduction in translation capacity, degradation of host mRNAs, and repression of nuclear mRNA export (Finkel et al., 2021a). Although several viral proteins were suggested to play a role in SARS-CoV-2-induced shutoff (Banerjee et al., 2020; Lei et al., 2020; Miorin et al., 2020; Shemesh et al., 2021; Vazquez et al., 2021), nsp1 is the best characterized shutoff factor. Furthermore, studies with mutants lacking nsp1 in mouse hepatitis virus (MHV) and in SARS-CoV illustrate nsp1 is a major pathogenesis factor of beta CoVs (Jimenez-Guardeño et al., 2015; Shen et al., 2019; Züst et al., 2007).

Fundamental early work on SARS-CoV nsp1 (Huang et al., 2011; Kamitani et al., 2006; Lokugamage et al., 2012; Narayanan et al., 2008) together with recent studies on SARS-CoV-2 nsp1 show that it interferes with host protein synthesis through several potentially distinct mechanisms. Nsp1 binds to the 40S ribosomal subunit, and its C-terminal domain physically blocks the mRNA entry channel, leading to reduction in translation both *in vitro* and in cells (Lapointe et al., 2021; Schubert et al., 2020; Thoms et al., 2020; Tidu et al., 2020; Yuan et al., 2020). However, the extent by which the virus overcomes this nsp1-mediated translational block and how nsp1's effects on translation come into play during infection remain largely unclear. SARS-CoV-2 nsp1 also promotes cellular mRNA degradation, and viral transcripts are refractory to these effects through their 5′ leader sequence (Finkel et al., 2021a; Mendez et al., 2021). Finally, nsp1 was also shown to interact with the export factor NXF1 and to

inhibit the nuclear export of cellular transcripts (Zhang et al., 2021). These findings portray complex interactions of nsp1 with the post-transcriptional life of mRNAs. Since there is extensive cross-talk between export, translation, and degradation, and perturbation of one can lead to indirect effects on the others, it remains critical to evaluate the extent by which nsp1 directly perturbs each of these functions and to measure the contribution of each function to nsp1 activity. Furthermore, since other viral proteins were suggested to interfere with cellular gene expression (Addetia et al., 2021; Banerjee et al., 2020; Hsu et al., 2021), and since host shutoff is thought to serve two independent purposes (to increase viral transcript translation and to inhibit the antiviral response), deciphering the role nsp1 plays in the context of infection represents a critical knowledge gap.

Here, we use overexpression of various nsp1 mutants to measure nsp1's effects on cellular gene expression. We illustrate that nsp1 mediates its function by accelerating mRNA degradation, inhibiting translation, and interfering with nuclear mRNA export, and these mechanisms are likely distinct and complementary. We further generated a SARS-CoV-2 mutant in which nsp1's ability to bind to the ribosome and to block translation and degrade cellular mRNAs is abolished. Using this mutant, we show that nsp1 is the main shutoff factor of SARS-CoV-2. We reveal that propagation of the mutant virus is inhibited *in vitro* in cells with functional interferon (IFN) pathway and *in vivo* in infected hamsters, and this attenuation is due to stronger IFN response. These results illustrate the critical and non-redundant role nsp1 plays in blocking the type I IFN response.

RESULTS

Nsp1 promotes both translation inhibition and decay of cellular mRNAs

We have previously demonstrated that, in addition to SARS-CoV-2 nsp1's ability to inhibit translation, it also promotes mRNA degradation (Finkel et al., 2021a). In SARS-CoV nsp1, ribosome binding as well as residues R124 and K125 are required for nsp1-induced host mRNA degradation activity (Kamitani et al., 2009; Lokugamage et al., 2012). Since nsp1 from SARS-CoV and SARS-CoV-2 are highly similar (84% identity in amino acids), we examined whether these residues are necessary for mRNA degradation also in SARS-CoV-2. We generated two nsp1 mutants: nsp1-ΔRB (RB stands for ribosome binding), in which we deleted amino acids 155–165, which are critical for nsp1's interactions with the ribosome (Schubert et al., 2020; Thoms et al., 2020; Tidu et al., 2020), and nsp1-CD (CD stands for cleavage defective), in which we mutated R124 and K125 to alanine (Figure 1A). We show that nsp1-wild type (WT), but not nsp1-ΔRB, associates with ribosomes (Figure 1B), as previously reported (Mendez et al., 2021; Schubert et al., 2020; Thoms et al., 2020). In agreement with a recent study (Mendez et al., 2021), nsp1-CD is still associated with ribosomes but to a lesser extent compared with nsp1-WT (Figure 1B). Notably, we noticed that nsp1 also likely represses its own expression, as the level of nsp1-WT was lower compared with the mutants (Figures 1B and S1A). To test the effects of these nsp1 mutants, we used two GFP reporters, one in which the GFP is fused to human beta-globin 5′ UTR (host-5′UTR-GFP) and a second in which it is fused to the viral 5′ leader sequence (CoV2-leader-GFP). These reporters were co-transfected with nsp1-WT, nsp1-ΔRB, nsp1-CD, or a control plasmid. Nsp1-WT and to a lesser extent nsp1-CD suppresses the expression of host-5′UTR-GFP, whereas nsp1-ΔRB had no major effect on GFP expression (Figure 1C). The GFP reduction mediated by nsp1-WT was associated with ~6-fold reduction in GFP mRNA levels, whereas the GFP mRNA levels were not affected by nsp1-ΔRB (Figure 1D), illustrating that, similarly to SARS-CoV nsp1 (Kamitani et al., 2009; Lokugamage et al., 2012), binding to the ribosome is critical for promoting RNA degradation. Furthermore, since nsp1-CD maintains the ability to suppress cellular RNA translation but does not lead to mRNA degradation, it indicates that translation inhibition and RNA degradation represent two distinct activities. In agreement with previous findings (Finkel et al., 2021a; Mendez et al., 2021; Tidu et al., 2020), nsp1-WT did not inhibit, and even slightly increased, the level of CoV2-leader-GFP, and nsp1-CD represses GFP expression, even when it is fused to the CoV2-leader (Figure 1E). Analysis of RNA expression demonstrated that CoV2-leader-GFP was refractory to nsp1-WT-induced degradation (Figure 1F).

We next examined the effect of nsp1 and its mutants on internal ribosome entry site (IRES)-mediated translation. We used a bicistronic mRNA, in which expression of the *Renilla* luciferase is mediated by cap-dependent translation and expression of *firefly* luciferase is driven by encephalomyocarditis virus (EMCV) IRES (Figure 1G). Nsp1-WT and to a lesser extent nsp1-CD, but not nsp1-ΔRB, suppressed the production of both luciferases, indicating nsp1 inhibits both capped as well as IRES-driven translation (Figure 1G). Furthermore, nsp1-WT, but not nsp1-ΔRB or nsp1-CD, induced a detectable endonucleolytic cleavage of the mRNA (Figure 1H). These results show that SARS-CoV-2 nsp1 blocks translation and induces an endonucleolytic cleavage of cellular RNAs that likely leads to their degradation. Nsp1 binding to the ribosome is essential for both these activities, and the translation inhibition and endonucleolytic RNA cleavage activities likely represent separable functions of nsp1.

Nsp1 inhibits nuclear mRNA export independently of its ribosome binding

Nsp1 was also demonstrated to block nuclear mRNA export through interaction with NXF1 (Zhang et al., 2021). Notably, the interaction with NXF1 was mapped to the N-terminal region of nsp1 (amino acids 1–129; Figure 1A) and therefore is likely independent of nsp1 binding to the ribosome (Zhang et al., 2021). To examine whether nsp1 affects mRNA export and whether this activity is maintained in the absence of ribosome binding, we transfected 293T cells with plasmids expressing nsp1-WT, nsp1-ΔRB, or a control plasmid and assessed the subcellular localization of polyadenylated transcripts by cytoplasmic and nuclear (cyto/nuc) fractionation followed by RNA sequencing (RNA-seq). Fractionation efficiencies were confirmed by comparing expression values of known nuclear and cytoplasmic RNAs (Figures S1B and S1C). In addition, we obtained a strong correlation between our cyto/nuc measurements and measurements conducted previously in a different cell type (Figure S1D). In agreement with nsp1 inhibiting mRNA export, nsp1-WT

CellPress
OPEN ACCESS

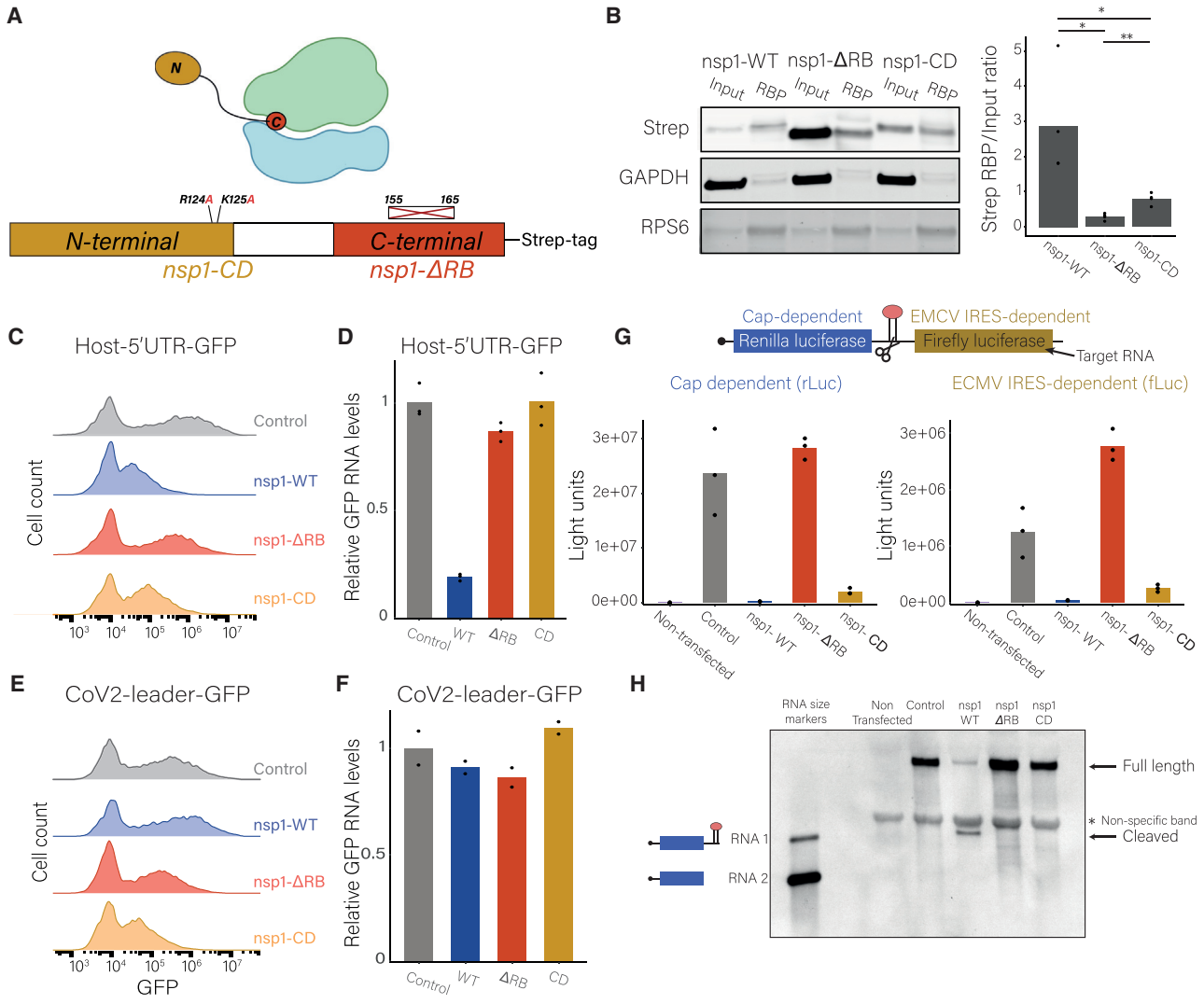

Figure 1. Nsp1 promotes both translation inhibition and decay of cellular mRNAs

(A) Schematic illustration of the nsp1-ΔRB and nsp1-CD mutations.

(B) 293T cells were transfected with nsp1-WT, nsp1-ΔRB, or nsp1-CD, and ribosomes were pelleted. Nsp1 protein levels in the input and in the ribosome pellet (RBP) were measured by western blot with Strep-Tactin. RPS6 and GAPDH were used as ribosomal protein and loading controls, respectively. Right panel presents the ratio of the strep signal in the RBP to input. Data points represent four replicates; *$p < 0.05$ and **$p < 0.01$ for a two-tailed t test.

(C–F) 293T cells co-transfected with nsp1-WT, nsp1-ΔRB, nsp1-CD, or a control plasmid together with (C and D) a reporter plasmid host-5′UTR-GFP or (E and F) the CoV2-leader-GFP. (C and E) GFP expression was measured by flow cytometry. (D and F) Relative GFP mRNA levels were measured by real-time PCR. 18S ribosomal RNA was used for normalization; two or three replicates are presented.

(G and H) Vero E6 cells were co-transfected with the reporter plasmid containing a cap-dependent *Renilla luciferase* followed by an EMCV IRES and *Firefly luciferase* along with an empty vector as a control or nsp1-WT, nsp1-ΔRB, or nsp1-CD. (G) Luciferase expression levels are shown. y axis represents light units; three replicates are presented. (H) RNAs were extracted and analyzed by northern blot using a digoxigenin-labeled rLuc riboprobe. RNA size marker is a mixture of *in vitro* transcribed RNA transcripts, RNA 1 and RNA 2, as shown.

expression led to relative nuclear enrichment of cellular transcripts (Figure 2A). Furthermore, this enrichment did not depend on nsp1-mediated induction of mRNA degradation, as nsp1-ΔRB expression also led to relative nuclear enrichment, and this effect was even stronger than that of nsp1-WT. The stronger effect was unexpected but could be attributed to the higher expression of nsp1-ΔRB as compared with nsp1-WT, due to the self-inhibitory effect nsp1 has on its own expression (Figure S1A). Indeed, analysis of the RNA-seq data showed that nsp1-ΔRB expression was 12-fold higher compared with nsp1-WT (Figure S1E). Furthermore, it is possible that, in the absence of binding to the ribosome, a higher proportion of nsp1 was free to interact with NXF1. Altogether, these measurements show that nsp1 is able to target three distinct steps in the mRNA biogenesis pathway and that nsp1's ability to inhibit mRNA export does not depend on its binding to the ribosome.

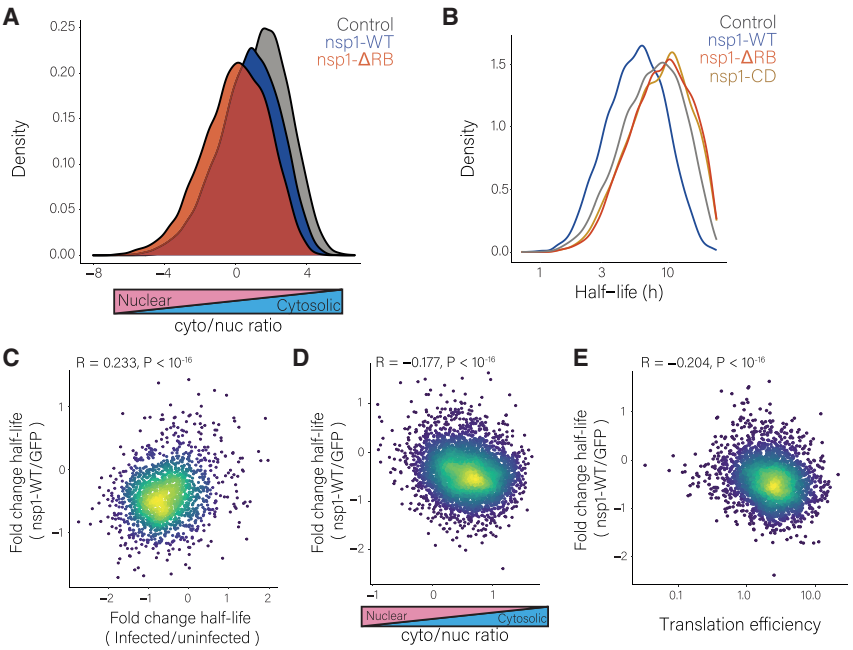

Figure 2. Nsp1 inhibits nuclear mRNA export and accelerates the decay of cytosolic mRNAs

(A) Distribution of the cytosolic to nuclear ratio of transcripts in 293T cells transfected with nsp1-WT, nsp1-ΔRB, or a control plasmid.

(B) Distribution of cellular transcript half-lives in 293T cells transfected with nsp1-WT, nsp1-ΔRB, nsp1-CD, or a control plasmid.

(C) Scatterplot of the fold change of transcript half-lives between SARS-CoV-2-infected and uninfected cells (Finkel et al., 2021a), relative to the fold change of 293T cells expressing nsp1-WT compared with a control.

(D and E) Scatterplots of the fold change of transcript half-lives between 293T cells expressing nsp1-WT compared with control relative to (D) cytosolic-to-nuclear ratio or (E) translation efficiency calculated by footprints divided by mRNA.

Nsp1 induces degradation of cytosolic transcripts

We next wanted to characterize the cellular transcripts that are sensitive to nsp1-induced degradation. Since we observed significant differences in the expression of nsp1-WT, nsp1-ΔRB, and nsp1-CD, due to the self-inhibitory effects of nsp1, we used the CoV2-5′ leader upstream of the various nsp1 proteins to confer protection from self-inhibition (Figure S2A).

To measure the induction of mRNA decay, we employed SLAM-seq (Herzog et al., 2017). This approach allows measurement of endogenous mRNA half-lives based on 4-thiouridine (4sU) incorporation into newly transcribed RNA. After RNA extraction, 4sU is converted to a cytosine analog using iodoacetamide, and these U to C conversions are identified and quantified by RNA-seq, providing means to quantify old and new mRNAs and to calculate mRNA decay (Finkel et al., 2021a; Herzog et al., 2017; Jürges et al., 2018). We applied SLAM-seq to 293T cells transfected with nsp1-WT, nsp1-CD, nsp1-ΔRB, or GFP as control (Figure S2B). We obtained all characteristics of high-quality SLAM-seq libraries: >8,000 quantified genes, U to C mutation rates starting at ∼1.5% and rising to ∼5.5%, and an increase with time in the portion of labeled RNA, which was stronger in cells expressing nsp1-WT, indicating a faster turnover of RNA in these cells (Figures S2C and S2D). There was a strong correlation between half-lives estimated from our SLAM-seq measurements and previous measurements (Figure S2E). Reassuringly, analysis of nsp1 expression from the RNA-seq reads demonstrated an equivalent expression of all constructs (Figure S2F). We observed a substantial reduction in cellular mRNA half-lives in cells expressing nsp1-WT, but not in cells expressing nsp1-ΔRB or nsp1-CD (Figure 2B), indicating significant induction of mRNA degradation only by nsp1-WT. Furthermore, we observed significant correlation between the profile of mRNA degradation that is induced by SARS-CoV-2 infection (Finkel et al., 2021a) and the degradation induced by nsp1-WT, but not by nsp1-ΔRB or nsp1-CD (Figures 2C, S3A, and S3B). This indicates that nsp1 plays a major role in inducing RNA degradation in infected cells. Expression of nsp1-WT, but not of nsp1-ΔRB or nsp1-CD, led to a more substantial reduction in the half-lives of cytoplasmic transcripts compared with transcripts that are mostly nuclear (Figures 2D and S3C–S3E). We also observed a significant correlation between the translation efficiency of cellular genes and their half-life reduction following nsp1-WT expression (Figures 2E and S3F). We analyzed the features of transcripts that are associated with sensitivity to nsp1-induced degradation, and cytosolic localization and translation efficiency showed the strongest correlation (Figure S3G). Overall, these findings demonstrate that the induction of mRNA degradation is a distinct function of nsp1, which is independent of export inhibition, and is mainly directed at cytosolic mRNAs that are engaged with the ribosome.

SARS-CoV-2 with a mutated nsp1 is attenuated in IFN competent cells

To evaluate the molecular and biological functions of nsp1 in infected cells, we generated a SARS-CoV-2 mutant, in which amino acids 155–165 of nsp1 were deleted (CoV2-mut). This mutant is similar to the nsp1-ΔRB in the expression studies described above. Deep sequencing confirmed the introduced deletion (Figure S4A), and there were no additional nucleotide alterations along the SARS-CoV-2 genome. Our initial characterization of the CoV2-mut was conducted in Vero E6 cells, which are type I IFN deficient (Emeny and Morgan, 1979). Cells infected with WT SARS-CoV-2 (CoV2-WT) or CoV2-mut expressed similar levels of nsp1 protein (Figure 3A), confirming that the deletion in nsp1 did not alter its expression. The majority of the nsp1-WT and nsp1-ΔRB accumulated in the cytoplasm in infected cells, but nsp1-ΔRB also showed perinuclear localization (Figure 3B), potentially reflecting stronger engagement with the

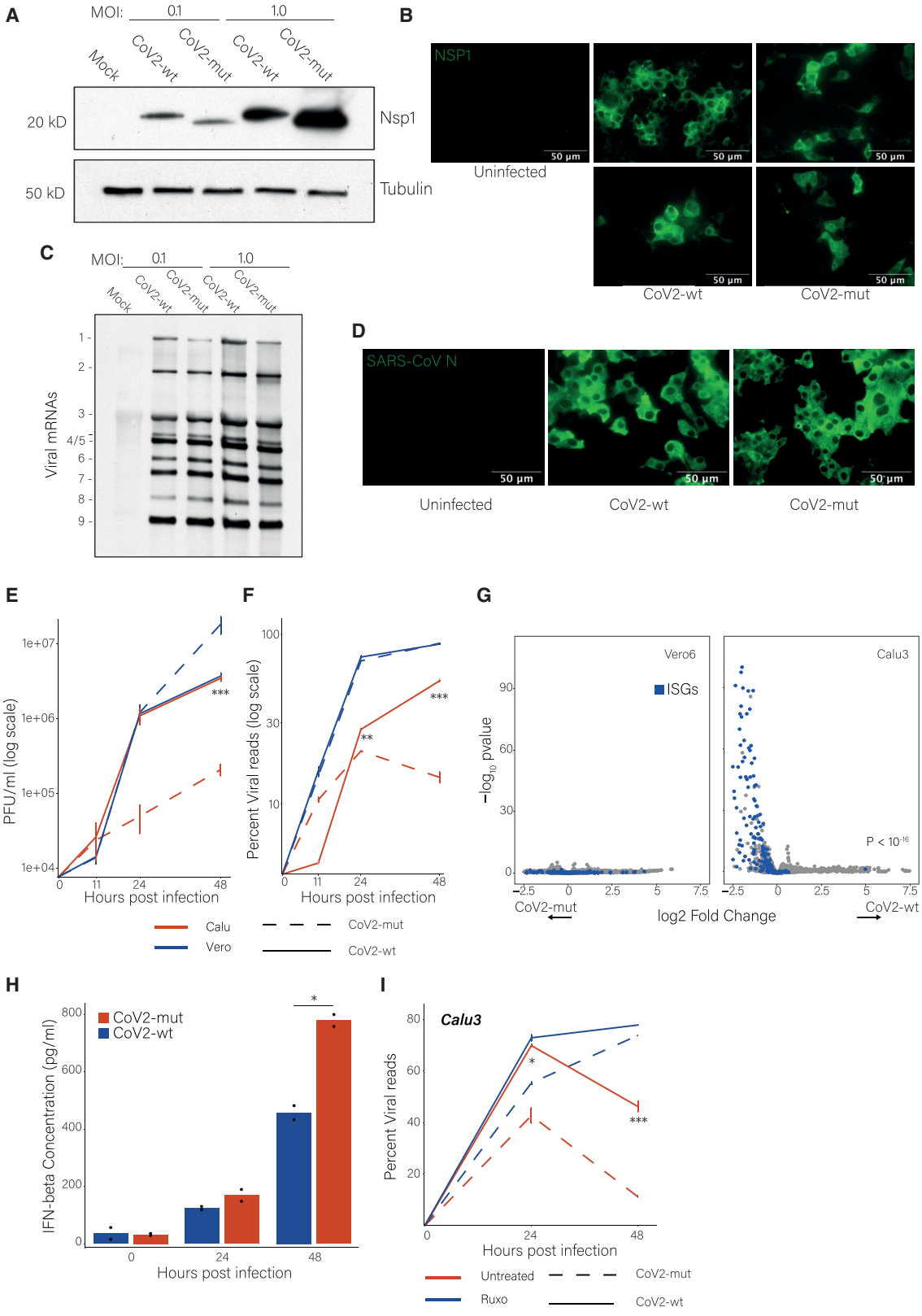

(legend on next page)

nuclear export machinery in the absence of ribosome binding. Infection with CoV2-mut or CoV2-WT resulted in comparable levels of accumulation of viral mRNAs at 18 h post-infection (hpi) (Figure 3C) as well as the expression of the viral N protein (Figure 3D). These experiments illustrate that infection of Vero E6 cells with CoV2-mut and CoV2-WT resulted in comparable levels of viral gene expression.

Next, we analyzed the propagation of CoV2-mut and CoV2-WT in both Vero E6 cells and Calu3 cells, the latter of which has an intact IFN response. In Vero E6 cells, titers of CoV2-mut were overall similar to that of CoV2-WT and at 48 hpi were even slightly higher (Figure 3E). In contrast, in Calu3 cells, at 24 and 48 hpi, the viral titers of CoV2-mut were lower compared with CoV2-WT (Figure 3E). This attenuation of CoV2-mut growth in Calu3 cells was also observed at a longer time course at a lower multiplicity of infection (MOI) (Figure S4B). Consistent with the growth kinetics, analysis of viral gene expression using RNA-seq shows comparable levels of viral RNAs in CoV2-WT- and CoV2-mut-infected Vero E6 cells, whereas in Calu3 cells, despite similar levels of viral RNAs initially, at 24 and 48 hpi, viral gene expression was lower for CoV2-mut (Figure 3F). As the inhibition of the IFN response is critical for optimal SARS-CoV-2 replication, we speculated that these cell-type-specific differences are due to the ability of nsp1 to interfere with the IFN response. Indeed, analysis of changes in cellular gene expression showed a stronger induction of IFN-stimulated genes (ISGs) in Calu3 cells infected with CoV2-mut compared with those infected with CoV2-WT ($p = 1.55 \times 10^{-114}$; Figure 3G), whereas no differences were observed in infected Vero E6 cells (Figure 3G). To confirm that the observed inhibition in the growth of CoV2-mut in Calu3 cells is indeed due to a more potent type I IFN response, we measured IFNβ protein levels in the supernatant of Calu3 cells infected with CoV2-mut or CoV2-WT. In the supernatant of cells infected with CoV2-WT, IFNβ levels were significantly lower than that of CoV2-mut (Figure 3H), illustrating the critical role of nsp1 in blocking type I IFN secretion. Furthermore, we tested whether the inhibition of IFN signaling by ruxolitinib (a selective JAK-STAT inhibitor; Jackson et al., 2016), can rescue CoV2-mut propagation in Calu3 cells. Indeed, CoV2-mut replication, as measured by analysis of RNA accumulation, was significantly enhanced by ruxolitinib treatment, whereas the impact on CoV2-WT replication was less prominent (Figure 3I). Overall, these results demonstrate that an enhanced IFN response in cells infected with CoV2-mut is responsible for its impaired propagation.

Nsp1's effect on viral RNA translation in infected cells

To gain insights into the molecular mechanisms that drive the functional differences between CoV2-WT and CoV2-mut, we assessed the changes in viral and host translation as well as RNA expression during infection with these two viruses. We infected Calu3 cells with either CoV2-WT or CoV2-mut at an MOI of 3, resulting in infection of the vast majority of the cells and thus a mostly synchronous cell population. In accordance with the early time points of growth kinetics in Calu3 (Figures 3E and 3F), at 8 hpi, there were no substantial differences in the infection of the two viruses (Figure S4C), allowing for direct molecular dissection of the nsp1's effect on cellular and viral gene expression.

We first examined how CoV2-WT and CoV2-mut affect global translation levels. We measured the levels of nascent protein synthesis using a tagged analogue of puromycin, O-propargyl puromycin (OPP), which is incorporated into nascent polypeptides. Calu3 cells were mock-infected or infected with CoV2-WT or CoV2-mut and nascent protein synthesis levels were measured at 4, 5, and 7 hpi. CoV2-WT infection led to a significant reduction in global translation levels already at 4 hpi, the effect of which was augmented over time, and at 7 hpi, the translation activity was reduced by 4-fold (Figure 4A). In contrast, CoV2-mut infection had no major effect on the overall translation levels in infected cells (Figure 4A). These results illustrate that nsp1 is the main driver of translation shutoff during SARS-CoV-2 infection and that this effect is mediated by its binding to the ribosome.

The OPP-labeling experiments provide an absolute measure of translation; however, they do not indicate the proportion of the translation capacity that is dedicated to the translation of viral genes. In order to gain a detailed view on the relative levels of viral and host translation, we harvested mock-infected and infected cells at 4 and 7 hpi for RNA-seq and ribosome profiling analysis. Metagene analysis, in which gene profiles are aligned and then averaged, revealed the expected profiles of ribosome footprints and mRNAs (Figures S5A and S5B). Using this data, we quantitatively assessed the expression pattern of cellular and viral transcripts. In order to evaluate the ability of SARS-CoV-2 to co-opt the host ribosomes, we calculated the

Figure 3. CoV2-mut is attenuated specifically in IFN competent cells

(A) Western blot analysis for nsp1 in Vero E6 cells infected with the CoV2-wt or the CoV2-mut at an MOI of 0.1 or 1.

(B) Vero E6 cells infected with CoV2-wt or CoV2-mut at 16 hpi (MOI = 2) and stained for Nsp1.

(C) Northern blot analysis using a probe for the common 3′ UTR of viral mRNAs, in Vero E6 cells infected with the CoV2-wt or the CoV2-mut at MOI of 0.1 or 1 at 18 hpi.

(D) Vero E6 cells infected with CoV2-wt or CoV2-mut and stained for the nucleocapsid protein.

(E and F) Viral titers (E) or percentage of viral reads (F) in Calu3 or Vero E6 cells infected with CoV2-wt or CoV2-mut at 0, 11, 24, and 48 hpi (MOI = 0.01). Three replicates for titers and two replicates for % of viral reads are presented. Mean and standard deviation (SD) are shown.

(G) Volcano plots showing changes in cellular transcript levels in CoV2-wt- versus CoV2-mut-infected Calu3 (right) or Vero E6 (left) cells at 24 hpi. The fold change and statistical significance are presented in the x axis and y axis, respectively. ISGs are marked in blue.

(H) IFN-beta concentrations measured by ELISA in the supernatant of Calu3 cells infected with CoV2-wt or CoV2-mut (MOI = 0.1) at 0, 24, and 48 hpi. Two replicates are presented.

(I) Percentage of viral reads in untreated or ruxolitinib-treated Calu3 cells infected with CoV2-wt or CoV2-mut at 0, 24, and 48 hpi (MOI = 0.01); two replicates are presented. The significance of the effect of ruxolitinib treatment on CoV2-mut compared with CoV2-wt was calculated using linear regression.

For all figures, *$p < 0.05$, **$p < 0.01$, and ***$p < 0.001$. Mean and SD are shown.

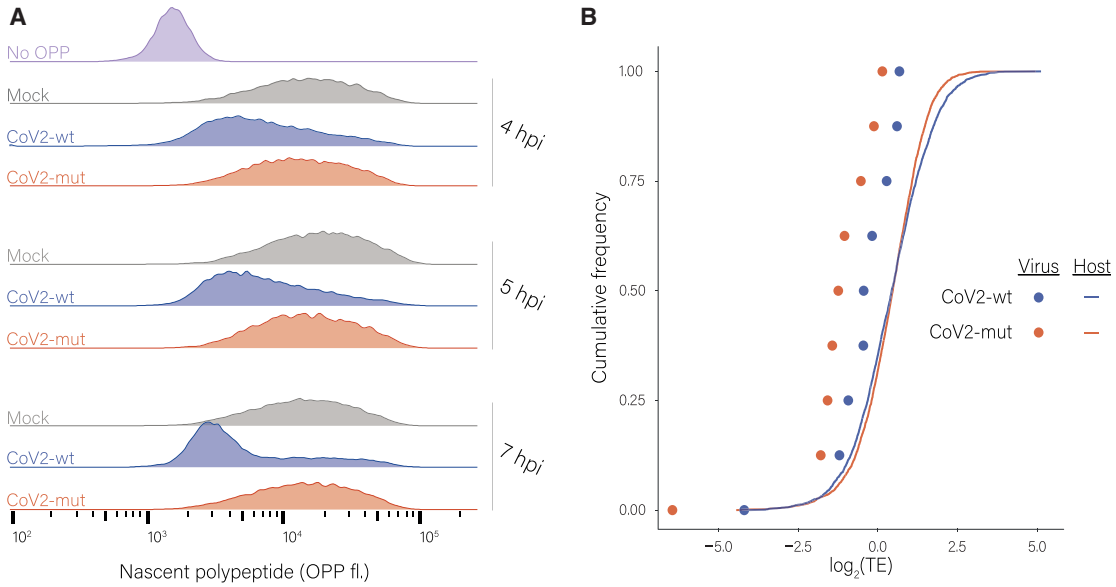

Figure 4. Effects of nsp1 on translation of viral and host mRNAs

(A) Calu3 cells infected with CoV2-wt or with CoV2-mut (MOI = 3) for 4, 5, and 7 hpi or an uninfected control following O-propargyl puromycin (OPP) incorporation, fluorescent labeling using click chemistry, and flow cytometry analysis.

(B) Cumulative frequency of human (line) and viral (dots) mRNAs according to their relative translation efficiency (TE) in cells infected with CoV2-wt (blue) or CoV2-mut (red) at 4 hpi. Each dot represents one of nine major viral mRNA species.

translation efficiency (TE) (ratio of footprints to mRNAs) of viral and cellular mRNAs in infected cells. We then compared the TE of human genes with that of viral genes at each time point with each virus. The analysis shows that, when cells are infected with CoV2-WT, viral genes' TEs fall within the low range of cellular gene TEs (Figures 4B and S5C). This could be attributed to the sequestration of vast amounts of viral RNA in double-membrane replication compartments, rendering them inaccessible to the ribosomes (Wolff et al., 2020) . Importantly, in cells infected with CoV2-mut, especially at 4 hpi, viral genes' TEs relative to cellular genes were further reduced (Figures 4B and S5C). This relative reduction in viral mRNA translation indicates that in infected cells nsp1, through its binding to the ribosome, specifically promotes viral mRNA translation . However, it is important to note that, in absolute terms, in cells infected with CoV2-WT, the overall translation levels are reduced by approximately 4-fold compared with cells infected with CoV2-mut (Figure 4A), and that ribosome-profiling-based measurements provide only relative values of translation. Therefore, it is likely that the absolute translation of viral genes in cells infected with CoV2-mut was comparable or even higher than the translation of viral genes in cells infected with CoV2-WT.

Nsp1 induces cellular mRNA degradation during SARS-CoV-2 infection

We next examined the changes in cellular and viral mRNA levels during SARS-CoV-2 infection. To estimate mRNA levels, we quantified the levels of rRNA and of total RNA extracted from uninfected Calu3 cells and from cells infected with CoV2-WT or CoV2-mut. We observed no substantial differences in either total RNA levels or in rRNA levels (Figures S6A–S6D). Subsequently, we sequenced total intracellular RNAs, without rRNA depletion, to assess the relative abundance of cellular and viral mRNAs in uninfected and infected Calu3 cells. We found that, during infection with CoV2-mut, viral transcripts are produced to comparable levels as CoV2-WT (Figure 5A). However, infection with CoV2-WT, but not CoV2-mut, is associated with an ~2-fold reduction in cellular mRNAs (Figure 5A). These results indicate that, during infection with CoV2-mut, the production of viral RNA is maintained, but there is no major interference in cellular RNA expression. Since nsp1-mediated mRNA degradation occurs in the cytosol, we examined whether the reduction in cellular RNA levels is associated with their subcellular localization. Indeed, compared with infection with CoV2-mut, CoV2-WT led to stronger reduction of transcripts that localize to the cytoplasm ($p = 5.2 \times 10^{-318}$; Figure 5B).

To directly measure the role of nsp1-ribosome binding in the induction of mRNA decay in infected cells, we applied SLAM-seq on uninfected cells and on cells infected with CoV2-WT or CoV2-mut. We obtained all characteristics of high-quality SLAM-seq libraries (Figures S7A and S7B) and a strong correlation with our previous measurements of mRNA half-life (Figures S7C and S7D). Importantly, we observed a substantial reduction in cellular mRNA half-lives upon infection with CoV2-WT, whereas the mRNA half-lives in CoV2-mut-infected cells were comparable to the levels measured in mock-infected cells (Figures 5C, 5D, and S7E). Furthermore, the reduction in half-life correlated both with cytosolic localization (Figures 5E, 5F, S7F, and S7G) as well as with the translation efficiency (Figures 5G, 5H, S7H, and S7I) in cells infected with CoV2-WT, but not with

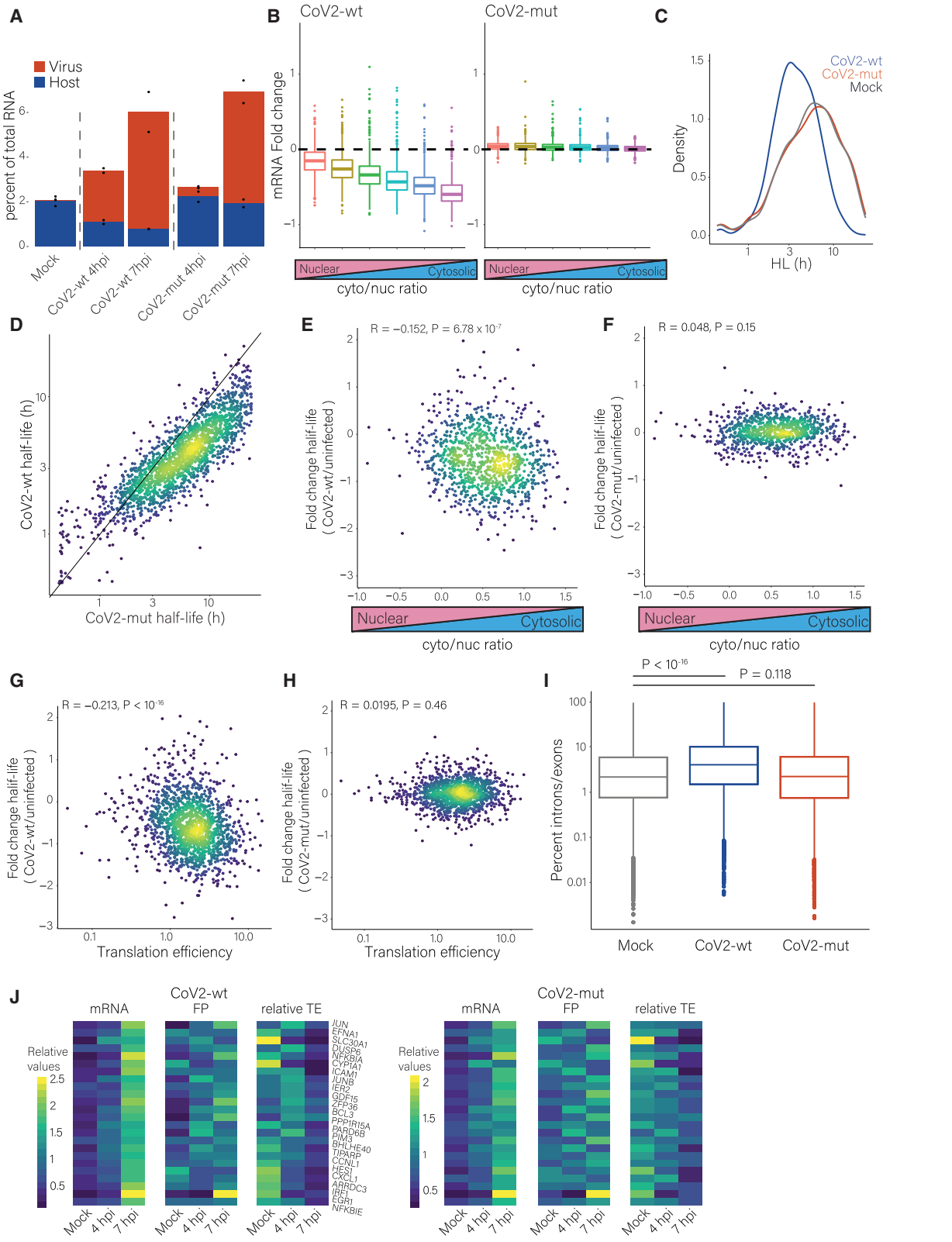

(legend on next page)

CoV2-mut. Together, these findings demonstrate that the degradation of cellular mRNAs during SARS-CoV-2 infection is mediated by nsp1 and is dependent on its interaction with the ribosome.

We previously observed that SARS-CoV-2 infection led to increased levels of intronic reads relative to exonic reads. However, much of this relative increase may be explained by massive degradation of mature cytosolic mRNAs (Finkel et al., 2021a), and it remains unclear whether SARS-CoV-2 directly inhibits splicing as was suggested (Banerjee et al., 2020). We therefore examined our data to assess whether increased intronic reads are still detected in cells infected with CoV2-mut, where there is no substantial RNA degradation. While infection with CoV2-WT led to a relative increase in intronic reads, infection with CoV2-mut did not (Figure 5I). These results imply that the relative increase in intronic reads during SARS-CoV-2 infection is largely driven by the accelerated degradation of mature cytosolic cellular transcripts by nsp1.

We previously demonstrated that mRNAs whose expression is induced in response to infection did not show a corresponding increase in ribosome footprints, and we ascribed this inability to engage with ribosomes to the inhibition of nuclear mRNA export in SARS-CoV-2-infected cells (Finkel et al., 2021a). Inhibition of nuclear mRNA export by SARS-CoV-2 was also demonstrated in additional studies with suggested involvement of ORF6 and nsp1 (Addetia et al., 2021; Burke et al., 2021; Zhang et al., 2021). Analysis of our mRNA and footprint measurements from infected cells revealed the same signature, and this occurred with both CoV2-WT and CoV2-mut (Figure 5J). This supports that inhibition of nuclear mRNA export represents a distinct function of nsp1 that is independent of its ability to induce mRNA degradation and translation inhibition.

As we demonstrated that the phenotypic growth defect of CoV2-mut virus in type I IFN-competent cells is specifically due to the role of nsp1 in blocking the IFN response, we analyzed the changes in expression and translation of IFN transcripts and ISGs in cells infected with CoV2-WT and CoV2-mut. We obtained an extremely low number of reads from IFN transcripts due to its low expression in both CoV2-WT and CoV2-mut infected cells, but the reduction in the translation and expression of ISGs was comparable to the reduction of other cellular mRNAs (Figures S7J and S7K). Altogether, these findings show that nsp1, through induction of mRNA degradation and inhibition of translation, drives host shutoff during SARS-CoV-2 infection. Although nsp1's functional importance lies specifically in blocking the IFN response, its degradation and translation inhibition activities are broad and affect the translating cytosolic mRNAs.

Nsp1 plays a critical role in SARS-CoV-2 pathogenesis *in vivo*

To examine the role of nsp1 in SARS-CoV-2 pathogenesis, we utilized the Syrian hamster model, which is susceptible to SARS-CoV-2 infection and exhibits symptoms that are comparable to those observed in humans (Francis et al., 2021; Sia et al., 2020). We infected two groups of eight hamsters with CoV2-WT or with CoV2-mut. We measured the weight of the hamsters daily and collected lung and nasal turbinate (NT) tissues at 3 and 7 days post-infection (dpi). Hamsters infected with CoV2-mut did not exhibit a significant change in body weight compared with uninfected hamsters, while CoV2-WT-infected hamsters began exhibiting a gradual decrease in body weight from day 2, reaching a statistically significant difference compared with CoV2-mut-infected hamsters at days 6 and 7 (Figure 6A).

We next quantified the viral titers in lungs and NT of hamsters from both groups. In agreement with the differences in weight loss, at 3 dpi, viral titers were significantly lower in the CoV2-mut-infected hamsters compared with the CoV2-WT-infected hamsters in both the lung and NT (Figure 6B). At 7 dpi, the virus was below the threshold of detection in CoV2-mut-infected tissues, whereas CoV2-WT virus was still significantly detected (Figure 6C).

The lungs of infected hamsters were also analyzed by immunohistochemistry (IHC) staining for the spike protein (Figure 6D). At 3 dpi, CoV2-mut infections were mostly restricted to the epithelial cells of the bronchioles, with minimal staining within the alveoli. In contrast, CoV2-WT infections were not restricted, extending from the bronchioles to the alveoli. In agreement with viral titers measurements, all specimens had less viral staining at 7 dpi than at 3 dpi, indicating resolution of viral infection. While viral infection remained detectable at 7 dpi within the lungs of CoV2-WT-challenged hamsters, the infection was largely restricted to the bronchioles. The CoV2-mut 7-dpi specimens appeared to have almost recovered from infection, while the virus antigen was still detectable and was restricted to the apical surface of the epithelia.

We also used RNA-seq to analyze the differences in viral propagation and immune response in the lungs at 3 dpi. CoV2-mut-infected hamsters exhibited an ~3-fold decrease in the percentage of viral RNA out of the entire mRNA pool, when compared with CoV2-WT (0.22% compared with 0.69%), further supporting that CoV2-mut propagation, *in vivo*, is inhibited. To

Figure 5. Nsp1 mediates cellular RNA degradation during SARS-CoV-2 infection

(A) Percentage of human or viral transcripts out of total RNA reads. Two replicates are presented.

(B) The fold change in RNA levels in CoV2-wt-infected (left) or CoV2-mut-infected (right) cells relative to uninfected cells at 7 hpi. Transcripts were grouped into six bins based on their cytosol-to-nucleus localization.

(C) The distribution of cellular transcript half-lives in uninfected or CoV2-wt- or CoV2-mut-infected cells as was determined by SLAM-seq.

(D) Scatterplot of cellular transcript half-lives in CoV2-wt- relative to CoV2-mut-infected cells.

(E–H) The fold change in transcript half-lives between CoV2-wt- (E and G) or CoV2-mut (F and H)-infected cells and uninfected cells, relative to the cytosol-to-nucleus ratio (E and F) or translation efficiency (G and H). Pearson's *R* and two-sided p values are presented.

(I) The ratio of intronic to exonic reads in uninfected or CoV2-wt- or CoV2-mut-infected cells at 4 hpi.

(J) Heatmaps showing the relative mRNA, footprints, and translation efficiency at 4 and 7 hpi of cellular genes that were induced in infected cells.

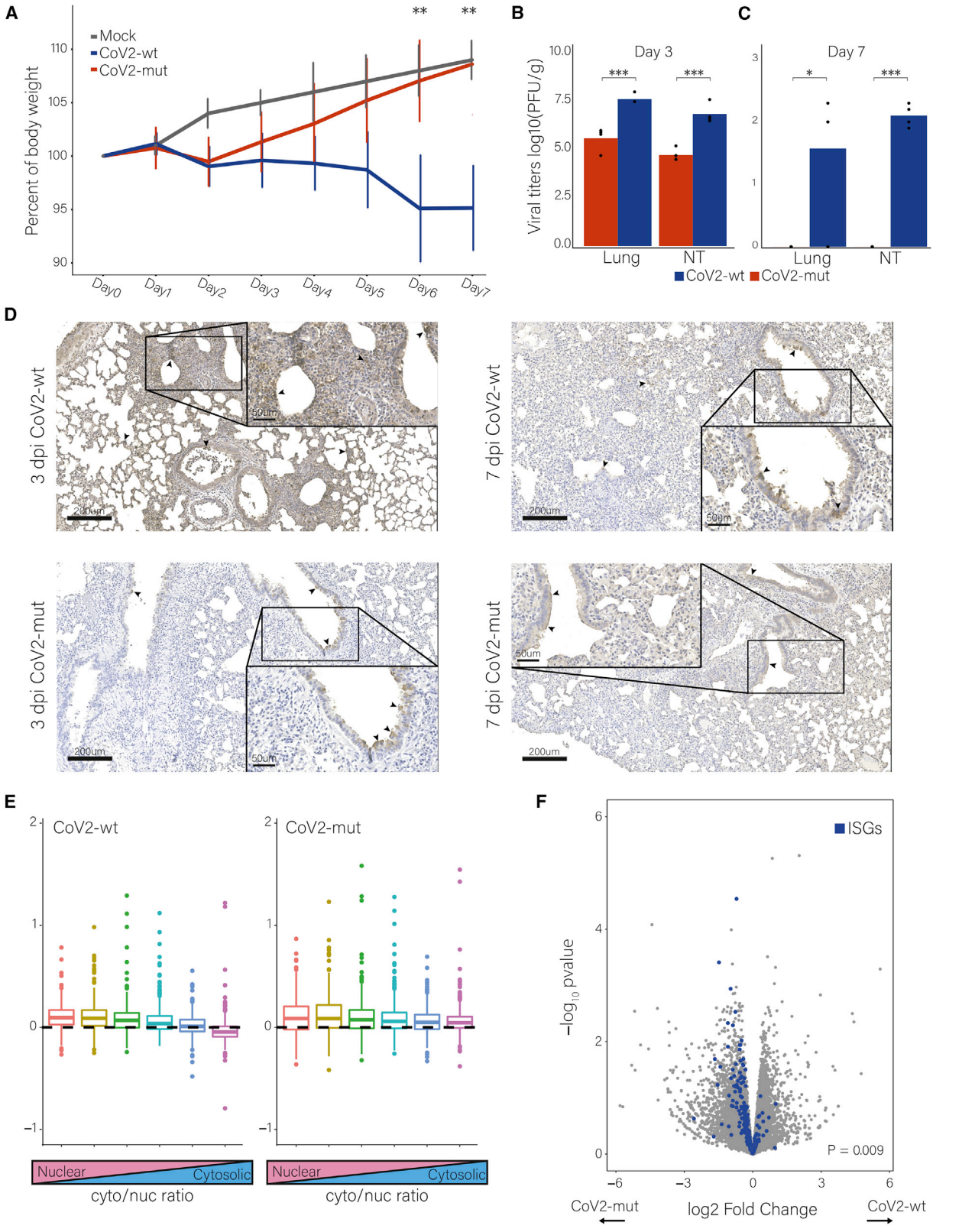

(legend on next page)

explore if evidence for nsp1-mediated mRNA degradation can be detected *in vivo*, we binned hamster transcripts according to the cyto/nuc ratio of their human homologs and analysed their change in expression. We found that, in infection with CoV2-WT and less with CoV2-mut, the transcripts that mostly localize to the cytoplasm were more reduced compared with transcripts that are more nuclear (Figure 6E), strongly indicating that nsp1-mediated mRNA degradation plays a major role *in vivo*.

Finally, differential expression analysis revealed a stronger upregulation of ISGs in the lungs of CoV2-mut-infected animals, compared with CoV2-WT-infected lungs ($p = 0.009$; Figure 6F). These data indicate that, in accordance with our findings *in vitro*, animals infected with CoV2-mut induced a stronger type I IFN response. Overall, these results show that nsp1, through its binding to the ribosome, plays a critical role in the SARS-CoV-2 life cycle and pathogenesis by interfering with host innate immune responses, facilitating the efficient propagation of the virus in the lungs.

DISCUSSION

Many viruses have developed varied and sophisticated mechanisms to repress host mRNA translation while concomitantly allowing the translation of viral mRNAs. In the case of SARS-CoV-2, several viral proteins have been suggested to interfere with cellular gene expression, including nsp1. We show here that nsp1 is responsible for the shutoff in protein synthesis during SARS-CoV-2 infection, and its activity is mediated by three distinct mechanisms: translation block, induction of mRNA degradation, and interference with nuclear mRNA export. Using reporters and broad measurements of changes in gene expression promoted by WT and nsp1-mutant viruses, we show that the degradation and translation-inhibition activities occur in the context of an nsp1-ribosome interaction, whereas the nuclear export inhibition activity does not significantly contribute to the global shutoff observed in infected cells and is independent from nsp1 binding to the ribosome.

Despite numerous studies, it remains unclear how viral transcripts overcome nsp1-mediated translation suppression and specifically how this evasion relates to the translation and degradation activities of nsp1. Our results show that, in the setting of overexpression, nsp1-CD, which does not lead to mRNA degradation, inhibits translation to a lesser extent than nsp1-WT, thus suggesting that both the translation inhibition and the mRNA degradation contribute to nsp1's ability to shut off cellular protein synthesis. The viral 5′ leader sequence, which is shared by all viral transcripts, allows transcripts to evade the inhibition imposed by nsp1 overexpression, but whether this reflects evasion from nsp1-induced degradation, block in translation, or evasion from both activities is harder to dissect. Our measurements, in combination with recent work (Finkel et al., 2021a; Mendez et al., 2021), show that the viral 5′ leader sequence makes mRNAs refractory to nsp1-mediated degradation. With regard to evasion from nsp1 translational block, two models could potentially explain viral mRNA escape. One posits that nsp1 blocks the translation of both cellular and viral transcripts, but since cellular transcripts are degraded, viral mRNAs remain the only available target for ribosomes that are not inhibited by nsp1. The other model proposes that viral mRNAs are refractory to translation suppression, as they interact with nsp1 in a manner that causes a change in its conformation, removing its C-terminal domain from the ribosome entry channel (Mendez et al., 2021; Shi et al., 2020; Tidu et al., 2020). These two models may not be mutually exclusive, and both mechanisms may contribute to the evasion of viral mRNAs from the translational block. The observation that nsp1-CD, which contains two point mutations in the N-terminal region, does not degrade cellular mRNAs, and in contrast to nsp1-WT also inhibits the translation of mRNA containing the viral 5′ leader sequence could be reconciled by both of these models. If these specific mutations affect the ability of nsp1 to recognize the viral 5′ leader sequence as was recently suggested (Mendez et al., 2021), it would explain why translation of viral mRNAs is inhibited by this nsp1 mutant. On the other hand, since nsp1-CD does not lead to cellular mRNA degradation, the enhanced competition for ribosomes that are not blocked by nsp1 can also contribute to reduction in viral translation.

Analysis of translation effeciency (the ratio of ribosome footprints to the number of RNA molecules) suggests that viral mRNAs are not efficiently translated compared with cellular transcripts. However, a major limitation of these measurements is that they rely on the sum of all viral RNA molecules. Viral RNA replication and transcription activities are highly efficient, and viral RNA synthesis occurs within a unique endomembrane system (Wolff et al., 2020) that would thus render much of the viral mRNAs inaccessible to ribosomes. This inaccessibility of potentially large portions of viral RNA likely skew our calculated translation efficiency. Comparing the translation efficiencies of viral and cellular transcripts in cells infected with CoV2-WT or with CoV2-mut allowed us to demonstrate nsp1 indeed specifically facilitates the translation of viral transcripts compared with cellular transcripts. However, at the same time, our measurements of the overall translation capacity in infected cells, using OPP incorporation into nascent chains, show that nsp1-WT leads to major reduction in the absolute levels of translation in

Figure 6. Nsp1 plays a critical role in SARS-CoV-2 pathogenesis *in vivo*

(A) Hamster weight as a percentage of their weight on day 0 for hamsters infected with CoV2-mut, CoV2-wt, and mock. Mean and SD are shown. $^{**}p < 0.01$.

(B and C) Viral titers in lungs and in NT at 3 dpi (B) and 7 dpi (C) for CoV2-wt- and CoV2-mut-infected hamsters. (A–C) Two-tailed t test is performed; $^{*}p < 0.05$ and $^{***}p < 0.001$. On days 0–3, eight replicates are presented. From day 4, four replicates are presented for the infected groups and eight for the control.

(D) IHC staining of lungs for spike (brown) with hematoxylin counterstain (blue) for hamsters infected with CoV2-wt or CoV2-mut at 3 dpi and 7 dpi. Arrows indicate select infected cells.

(E) The fold change in mRNA levels in CoV2-wt-infected (left) or CoV2-mut-infected (right) relative to mock-infected hamsters at 3 dpi. Transcripts were grouped into six bins based on their cytosol-to-nucleus ratio.

(F) Cellular transcript levels in CoV2-wt- versus CoV2-mut-infected hamsters at 3 dpi. The fold change and significance are presented in the x axis and y axis, respectively. ISGs are marked in blue. ISGs enrichment was calculated using a hypergeometric test. Two extreme genes were removed.

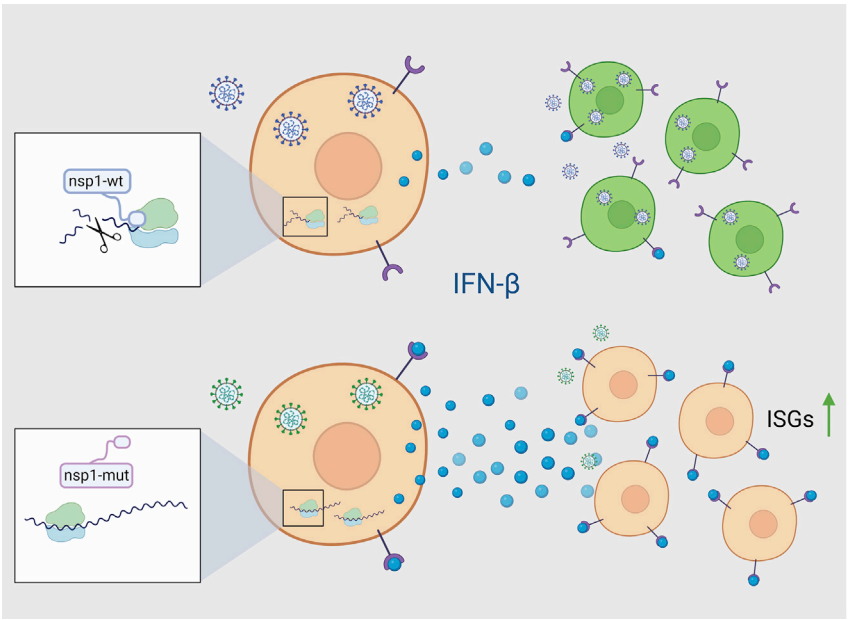

Figure 7. Proposed model for nsp1-mediated immune evasion

Nsp1 blocks translation and degrades cellular mRNAs, and this leads to global reduction in protein production, including reduction in the production of IFN-β. Infected and bystander neighboring cells are exposed to minimal amounts of IFN-β, and the virus can efficiently propagate. During CoV2-mut infection, nsp1 does not block the translation of cellular mRNAs and IFN-β is produced. ISGs expression is induced in infected and bystander neighboring cells, leading to reduction in viral propagation.

infected cells. Since the vast majority of mRNAs in infected cells are viral, it suggests that viral translation is also inhibited in the presence of nsp1. Together, these results support a model in which nsp1 acts as a strong inhibitor of translation through its tight interaction with ribosomes and thus inhibits the translation of both viral and cellular mRNAs. Viral transcripts, through their 5′ leader, could partially escape this translation repression. At the same time, ribosome-bound nsp1 also leads to an accelerated degradation of cellular, but not of viral, mRNAs, allowing viral mRNAs to quickly take over and dominate the mRNA pool.

We reveal here that, similarly to SARS-CoV nsp1 (Kamitani et al., 2009; Lokugamage et al., 2012), SARS-CoV-2 nsp1 likely induces an endonucleolytic cleavage of cellular mRNA that leads to their degradation. Our broad measurements show that nsp1 accelerates the degradation of cytosolic RNAs and specifically the ones that are more highly translated. Since nsp1 is physically bound to the ribosome and the degradation depends on this interaction, an appealing speculation is that nsp1 recruits a cellular endonuclease whose activity relates to mRNA translation surveillance. A major future challenge would be to identify this putative endonuclease.

Host shutoff is traditionally thought to contribute to viral propagation by facilitating viral protein translation and by blocking the ability of the cell to mount an efficient antiviral response. Our results illustrate that the main functional importance of host shutoff during SARS-CoV-2 infection is the latter. The observation that the CoV2-mut virus does not exhibit a substantial propagation defect in Vero cells and that, in the absence of functional nsp1, viral protein expression is intact points that the growth defect of CoV2-mut in type I IFN-competent cells and *in vivo* in infected hamsters is due to a more efficient IFN response in the absence of host shutoff.

We did not observe a major block in viral protein production during the first infection cycle with CoV2-mut in IFN-competent cells. This suggests that the defect observed in CoV2-mut propagation is likely due to the critical role of nsp1 in blocking type I IFN production, which then lead to differences in ISG induction in neighboring uninfected cells (Figure 7). Since SARS-CoV-2 is sensitive to IFN treatment (Mantlo et al., 2020), these differences in IFN production could explain the propagation defect of CoV2-mut.

Overall, our data establish that nsp1 is a major immune evasion factor of SARS-CoV-2. Although SARS-CoV-2 encodes additional inhibitors of the innate immune defenses (Xia et al., 2020), we show that a loss in nsp1 activity renders the virus vulnerable to immune response both *in vitro* in IFN-competent cells and *in vivo* in hamsters. Mechanistically, we illustrate that, in the context of infection, nsp1 mediates its functions through a broad induction of cellular mRNA degradation and translation inhibition. These functions are linked, and it is likely that both are major contributors to SARS-CoV-2 virulence.

Limitations of the study

While our measurements of nsp1-mediated inhibition of protein synthesis were absolute, calculations of translation efficiency are relative within each sample and rely on all mRNA molecules in the cells, regardless of their localization. For that reason, it is difficult to quantitatively assess the contribution of nsp1 to the translation of viral transcripts in the context of infection. An additional gap in deciphering the shutoff activity of nsp1 is the functional coupling between the translation block and RNA degradation, as the mutant we generated lacked both activities. We hypothesize that nsp1 recruits a cellular endonuclease to promote RNA cleavage, but future work will need to decipher the exact mechanism and to probe for the functional importance of this process.

STAR★METHODS

Detailed methods are provided in the online version of this paper and include the following:

- KEY RESOURCES TABLE
- RESOURCE AVAILABILITY
  - Lead contact

SUPPLEMENTAL INFORMATION

Supplemental information can be found online at https://doi.org/10.1016/j.celrep.2022.110954.

ACKNOWLEDGMENTS

We thank Igor Ulitsky and Schraga Schwartz for providing valuable feedback. We also thank Dr. Steve Widen at UTMB's Next Generation Sequencing Core for technical assistance. This work was supported by Public Health Service grant AI146081 from the National Institutes of Health and pilot grants from the Institute for Human Infections and Immunity at The University of Texas Medical Branch to S.M.; by the National Institute of Allergy and Infectious Diseases and the Center for Research on Influenza Pathogenesis (HHSN272201400008C), Research Program on Emerging and Re-emerging Infectious Diseases (JP20fk0108412), and the Japan Program for Infectious Diseases Research and Infrastructure (JP21wm0125002) from the Japan Agency for Medical Research and Development (AMED) to Y.K.; and by research grants from the Weizmann Corona Response Fund, the Knell Family Center for Microbiology, a research grant from the Weizmann SABRA - Yeda-Sela - WRC Program, the Estate of Emile Mimran and The Maurice and Vivienne Wohl Biology Endowment to N.S.-G.

AUTHOR CONTRIBUTIONS

T.F., A.G., K.N., N.S.-G., S.M., N.P., and Y.K. conceptualized the study; T.F., A.G., K.N., M.K., M.S., J.C.H., P.J.H., Y.Y.-R., H.T., S.W., C.-T.K.T., T.I., and N.P. performed experiments; T.F., A.G., A.N., K.N., M.K., J.C.H., P.J.H., C.-T.K.T., and Y.F. analyzed the data; and S.M., K.N., M.K., M.S., C.-T.K.T., N.S.-G., T.F., and A.G. wrote the manuscript with contribution from all other authors.

DECLARATION OF INTERESTS

The authors declare no competing interests.

Received: January 3, 2022
Revised: April 6, 2022
Accepted: May 23, 2022
Published: May 26, 2022

REFERENCES

Abernathy, E., and Glaunsinger, B. (2015). Emerging roles for RNA degradation in viral replication and antiviral defense. Virology *479-480*, 600–608. https://doi.org/10.1016/j.virol.2015.02.007.

Addetia, A., Lieberman, N.A.P., Phung, Q., Hsiang, T.-Y., Xie, H., Roychoudhury, P., Shrestha, L., Loprieno, M.A., Huang, M.-L., Gale, M., Jr., et al. (2021). SARS-CoV-2 ORF6 disrupts bidirectional nucleocytoplasmic transport through interactions with Rae1 and Nup98. mBio *12*, e00065-21. https://doi.org/10.1128/mbio.00065-21.

Banerjee, A.K., Blanco, M.R., Bruce, E.A., Honson, D.D., Chen, L.M., Chow, A., Bhat, P., Ollikainen, N., Quinodoz, S.A., Loney, C., et al. (2020). SARS-CoV-2 disrupts splicing, translation, and protein trafficking to suppress host defenses. Cell *183*, 1325–1339.e21. https://doi.org/10.1016/j.cell.2020.10.004.

Burke, J.M., St Clair, L.A., Perera, R., and Parker, R. (2021). SARS-CoV-2 infection triggers widespread host mRNA decay leading to an mRNA export block. RNA *27*, 1318–1329. https://doi.org/10.1261/rna.078923.121.

Carlevaro-Fita, J., Liu, L., Zhou, Y., Zhang, S., Chouvardas, P., Johnson, R., and Li, J. (2019). LnCompare: gene set feature analysis for human long non-coding RNAs. Nucleic. Acids. Res. *47*, W523–W529. https://doi.org/10.1093/nar/gkz410.

Dobin, A., Davis, C.A., Schlesinger, F., Drenkow, J., Zaleski, C., Jha, S., Batut, P., Chaisson, M., and Gingeras, T.R. (2013). STAR: ultrafast universal RNA-seq aligner. Bioinformatics *29*, 15–21. https://doi.org/10.1093/bioinformatics/bts635.

Emeny, J.M., and Morgan, M.J. (1979). Regulation of the interferon system: evidence that Vero cells have a genetic defect in interferon production. J. Gen. Virol. *43*, 247–252. https://doi.org/10.1099/0022-1317-43-1-247.

Finkel, Y., Schmiedel, D., Tai-Schmiedel, J., Nachshon, A., Winkler, R., Dobesova, M., Schwartz, M., Mandelboim, O., and Stern-Ginossar, N. (2020). Comprehensive annotations of human herpesvirus 6A and 6B genomes reveal novel and conserved genomic features. Elife *9*, e50960. https://doi.org/10.7554/elife.50960.

Finkel, Y., Gluck, A., Nachshon, A., Winkler, R., Fisher, T., Rozman, B., Mizrahi, O., Lubelsky, Y., Zuckerman, B., Slobodin, B., et al. (2021a). SARS-CoV-2 uses a multipronged strategy to impede host protein synthesis. Nature *594*, 240–245. https://doi.org/10.1038/s41586-021-03610-3.

Finkel, Y., Mizrahi, O., Nachshon, A., Weingarten-Gabbay, S., Morgenstern, D., Yahalom-Ronen, Y., Tamir, H., Achdout, H., Stein, D., Israeli, O., et al. (2021b). The coding capacity of SARS-CoV-2. Nature *589*, 125–130. https://doi.org/10.1038/s41586-020-2739-1.

Francis, M.E., Goncin, U., Kroeker, A., Swan, C., Ralph, R., Lu, Y., Etzioni, A.L., Falzarano, D., Gerdts, V., Machtaler, S., et al. (2021). SARS-CoV-2 infection in the Syrian hamster model causes inflammation as well as type I interferon dysregulation in both respiratory and non-respiratory tissues including the heart and kidney. PLoS Pathog. *17*, e1009705. https://doi.org/10.1371/journal.ppat.1009705.

Harcourt, J., Tamin, A., Lu, X., Kamili, S., Sakthivel, S.K., Murray, J., Queen, K., Tao, Y., Paden, C.R., Zhang, J., et al. (2020). Isolation and characterization of

SARS-CoV-2 from the first US COVID-19 patient. Preprint at bioRxiv. https://doi.org/10.1101/2020.03.02.972935.

Herzog, V.A., Reichholf, B., Neumann, T., Rescheneder, P., Bhat, P., Burkard, T.R., Wlotzka, W., von Haeseler, A., Zuber, J., and Ameres, S.L. (2017). Thiol-linked alkylation of RNA to assess expression dynamics. Nat. Methods *14*, 1198–1204. https://doi.org/10.1038/nmeth.4435.

Hsu, J.C.-C., Laurent-Rolle, M., Pawlak, J.B., Wilen, C.B., and Cresswell, P. (2021). Translational shutdown and evasion of the innate immune response by SARS-CoV-2 NSP14 protein. Proc. Natl. Acad. Sci. U S A *118*, e2101161118. https://doi.org/10.1073/pnas.2101161118.

Huang, C., Lokugamage, K.G., Rozovics, J.M., Narayanan, K., Semler, B.L., and Makino, S. (2011). SARS coronavirus nsp1 protein induces template-dependent endonucleolytic cleavage of mRNAs: viral mRNAs are resistant to nsp1-induced RNA cleavage. PLoS Pathog. *7*, e1002433. https://doi.org/10.1371/journal.ppat.1002433.

Irigoyen, N., Firth, A.E., Jones, J.D., Chung, B.Y.-W., Siddell, S.G., and Brierley, I. (2016). High-resolution analysis of coronavirus gene expression by RNA sequencing and ribosome profiling. PLoS Pathog. *12*, e1005473. https://doi.org/10.1371/journal.ppat.1005473.

Jackson, J.D., Markert, J.M., Li, L., Carroll, S.L., and Cassady, K.A. (2016). STAT1 and NF-κB inhibitors diminish basal interferon-stimulated gene expression and improve the productive infection of oncolytic HSV in MPNST cells. Mol. Cancer Res. *14*, 482–492. https://doi.org/10.1158/1541-7786.mcr-15-0427.

Jimenez-Guardeño, J.M., Regla-Nava, J.A., Nieto-Torres, J.L., DeDiego, M.L., Castaño-Rodriguez, C., Fernandez-Delgado, R., Perlman, S., and Enjuanes, L. (2015). Identification of the mechanisms causing reversion to virulence in an attenuated SARS-CoV for the design of a genetically stable vaccine. PLoS Pathog. *11*, e1005215. https://doi.org/10.1371/journal.ppat.1005215.

Jürges, C., Dölken, L., and Erhard, F. (2018). Dissecting newly transcribed and old RNA using GRAND-SLAM. Bioinformatics *34*, i218–i226. https://doi.org/10.1093/bioinformatics/bty256.

Kamitani, W., Narayanan, K., Huang, C., Lokugamage, K., Ikegami, T., Ito, N., Kubo, H., and Makino, S. (2006). Severe acute respiratory syndrome coronavirus nsp1 protein suppresses host gene expression by promoting host mRNA degradation. Proc. Natl. Acad. Sci. U S A *103*, 12885–12890. https://doi.org/10.1073/pnas.0603144103.

Kamitani, W., Huang, C., Narayanan, K., Lokugamage, K.G., and Makino, S. (2009). A two-pronged strategy to suppress host protein synthesis by SARS coronavirus Nsp1 protein. Nat. Struct. Mol. Biol. *16*, 1134–1140. https://doi.org/10.1038/nsmb.1680.

Kim, D., Lee, J.-Y., Yang, J.-S., Kim, J.W., Kim, V.N., and Chang, H. (2020). The architecture of SARS-CoV-2 transcriptome. Cellule *181*, 914–921.e10. https://doi.org/10.1016/j.cell.2020.04.011.

Langmead, B., et al. (2009). Ultrafast and memory-efficient alignment of short DNA sequences to the human genome. Genome biology, R25 (2009). https://doi.org/10.1186/gb-2009-10-3-r25.

Lapointe, C.P., Grosely, R., Johnson, A.G., Wang, J., Fernández, I.S., and Puglisi, J.D. (2021). Dynamic competition between SARS-CoV-2 NSP1 and mRNA on the human ribosome inhibits translation initiation. Proc. Natl. Acad. Sci. U S A *118*, e2017715118. https://doi.org/10.1073/pnas.2017715118.

Lei, X., Dong, X., Ma, R., Wang, W., Xiao, X., Tian, Z., Wang, C., Wang, Y., Li, L., Ren, L., et al. (2020). Activation and evasion of type I interferon responses by SARS-CoV-2. Nat. Commun. *11*, 3810. https://doi.org/10.1038/s41467-020-17665-9.

Lokugamage, K.G., Narayanan, K., Huang, C., and Makino, S. (2012). Severe acute respiratory syndrome coronavirus protein nsp1 is a novel eukaryotic translation inhibitor that represses multiple steps of translation initiation. J. Virol. *86*, 13598–13608. https://doi.org/10.1128/jvi.01958-12.

Love, M.I., Huber, W., and Anders, S. (2014). Moderated estimation of fold change and dispersion for RNA-seq data with DESeq2. Genome. Biol. *15*, 550. https://doi.org/10.1186/s13059-014-0550-8.

Mantlo, E., Bukreyeva, N., Maruyama, J., Paessler, S., and Huang, C. (2020). Antiviral activities of type I interferons to SARS-CoV-2 infection. Antiviral. Res. *179*, 104811. https://doi.org/10.1016/j.antiviral.2020.104811.

Mendez, A.S., Ly, M., González-Sánchez, A.M., Hartenian, E., Ingolia, N.T., Cate, J.H., and Glaunsinger, B.A. (2021). The N-terminal domain of SARS-CoV-2 nsp1 plays key roles in suppression of cellular gene expression and preservation of viral gene expression. Cell Rep. *37*, 109841. https://doi.org/10.1016/j.celrep.2021.109841.

Miorin, L., Kehrer, T., Sanchez-Aparicio, M.T., Zhang, K., Cohen, P., Patel, R.S., Cupic, A., Makio, T., Mei, M., Moreno, E., et al. (2020). SARS-CoV-2 Orf6 hijacks Nup98 to block STAT nuclear import and antagonize interferon signaling. Proc. Natl. Acad. Sci. U. S. A. *117*, 28344–28354. https://doi.org/10.1073/pnas.2016650117.

Nakagawa, K., and Makino, S. (2021). Mechanisms of coronavirus nsp1-mediated control of host and viral gene expression. Cells *10*, 300. https://doi.org/10.3390/cells10020300.

Nakagawa, K., Lokugamage, K.G., and Makino, S. (2016). Viral and cellular mRNA translation in coronavirus-infected cells. Adv. Virus. Res. *96*, 165–192. https://doi.org/10.1016/bs.aivir.2016.08.001.

Narayanan, K., Huang, C., Lokugamage, K., Kamitani, W., Ikegami, T., Tseng, C.-T.K., and Makino, S. (2008). Severe acute respiratory syndrome coronavirus nsp1 suppresses host gene expression, including that of type I interferon, in infected cells. J. Virol. *82*, 4471–4479. https://doi.org/10.1128/jvi.02472-07.

Narayanan, K., Ramirez, S.I., Lokugamage, K.G., and Makino, S. (2015). Coronavirus nonstructural protein 1: common and distinct functions in the regulation of host and viral gene expression. Virus. Res. *202*, 89–100. https://doi.org/10.1016/j.virusres.2014.11.019.

Schindelin, J., et al. (2012). Fiji: an open-source platform for biological-image analysis. Nature Methods. https://doi.org/10.1038/nmeth.2019.

Schubert, K., Karousis, E.D., Jomaa, A., Scaiola, A., Echeverria, B., Gurzeler, L.-A., Leibundgut, M., Thiel, V., Mühlemann, O., and Ban, N. (2020). SARS-CoV-2 Nsp1 binds the ribosomal mRNA channel to inhibit translation. Nat. Struct. Mol. Biol. *27*, 959–966. https://doi.org/10.1038/s41594-020-0511-8.

Shemesh, M., Aktepe, T.E., Deerain, J.M., McAuley, J.L., Audsley, M.D., David, C.T., Purcell, D.F.J., Urin, V., Hartmann, R., Moseley, G.W., et al. (2021). SARS-CoV-2 suppresses IFNβ production mediated by NSP1, 5, 6, 15, ORF6 and ORF7b but does not suppress the effects of added interferon. PLoS Pathog. *17*, e1009800. https://doi.org/10.1371/journal.ppat.1009800.

Shen, Z., Wang, G., Yang, Y., Shi, J., Fang, L., Li, F., Xiao, S., Fu, Z.F., and Peng, G. (2019). A conserved region of nonstructural protein 1 from alphacoronaviruses inhibits host gene expression and is critical for viral virulence. J. Biol. Chem. *294*, 13606–13618. https://doi.org/10.1074/jbc.ra119.009713.

Shi, M., Wang, L., Fontana, P., Vora, S., Zhang, Y., Fu, T.-M., Lieberman, J., and Wu, H. (2020). SARS-CoV-2 Nsp1 suppresses host but not viral translation through a bipartite mechanism. Preprint at bioRxiv. https://doi.org/10.1101/2020.09.18.302901.

Sia, S.F., Yan, L.-M., Chin, A.W.H., Fung, K., Choy, K.-T., Wong, A.Y.L., Kaewpreedee, P., Perera, R.A.P.M., Poon, L.L.M., Nicholls, J.M., et al. (2020). Pathogenesis and transmission of SARS-CoV-2 in golden hamsters. Nature *583*, 834–838. https://doi.org/10.1038/s41586-020-2342-5.

Stern-Ginossar, N., Thompson, S.R., Mathews, M.B., and Mohr, I. (2019). Translational control in virus-infected cells. Cold Spring Harb. Perspect. Biol. *11*, a033001. https://doi.org/10.1101/cshperspect.a033001.

Thoms, M., Buschauer, R., Ameismeier, M., Koepke, L., Denk, T., Hirschenberger, M., Kratzat, H., Hayn, M., Mackens-Kiani, T., Cheng, J., et al. (2020). Structural basis for translational shutdown and immune evasion by the Nsp1 protein of SARS-CoV-2. Science *369*, 1249–1255. https://doi.org/10.1126/science.abc8665.

Tidu, A., Janvier, A., Schaeffer, L., Sosnowski, P., Kuhn, L., Hammann, P., Westhof, E., Eriani, G., and Martin, F. (2020). The Viral Protein NSP1 Acts as a Ribosome Gatekeeper for Shutting Down Host Translation and Fostering SARS-CoV-2 Translation (RNA).

Tseng, C.-T.K., Huang, C., Newman, P., Wang, N., Narayanan, K., Watts, D.M., Makino, S., Packard, M.M., Zaki, S.R., Chan, T.-S., and Peters, C.J. (2007). Severe acute respiratory syndrome coronavirus infection of mice transgenic for the human angiotensin-converting enzyme 2 virus receptor. J. Virol. *81*, 1162–1173. https://doi.org/10.1128/jvi.01702-06.

Vazquez, C., Swanson, S.E., Negatu, S.G., Dittmar, M., Miller, J., Ramage, H.R., Cherry, S., and Jurado, K.A. (2021). SARS-CoV-2 viral proteins NSP1 and NSP13 inhibit interferon activation through distinct mechanisms. PLoS One *16*, e0253089. https://doi.org/10.1371/journal.pone.0253089.

Wolff, G., Limpens, R.W.A.L., Zevenhoven-Dobbe, J.C., Laugks, U., Zheng, S., de Jong, A.W.M., Koning, R.I., Agard, D.A., Grünewald, K., Koster, A.J., et al. (2020). A molecular pore spans the double membrane of the coronavirus replication organelle. Science *369*, 1395–1398. https://doi.org/10.1126/science.abd3629.

Xia, H., Cao, Z., Xie, X., Zhang, X., Chen, J.Y.-C., Wang, H., Menachery, V.D., Rajsbaum, R., and Shi, P.-Y. (2020). Evasion of type I interferon by SARS-CoV-2. Cell Rep. *33*, 108234. https://doi.org/10.1016/j.celrep.2020.108234.

Xie, X., Muruato, A., Lokugamage, K.G., Narayanan, K., Zhang, X., Zou, J., Liu, J., Schindewolf, C., Bopp, N.E., Aguilar, P.V., et al. (2020). An infectious cDNA clone of SARS-CoV-2. Cell Host Microbe *27*, 841–848.e3. https://doi.org/10.1016/j.chom.2020.04.004.

Yahalom-Ronen, Y., Tamir, H., Melamed, S., Politi, B., Shifman, O., Achdout, H., Vitner, E.B., Israeli, O., Milrot, E., Stein, D., et al. (2020). A single dose of recombinant VSV-ΔG-spike vaccine provides protection against SARS-CoV-2 challenge. Nat. Commun. *11*, 6402. https://doi.org/10.1038/s41467-020-20228-7.

Yoshikawa, N., Yoshikawa, T., Hill, T., Huang, C., Watts, D.M., Makino, S., Milligan, G., Chan, T., Peters, C.J., and Tseng, C.-T.K. (2009). Differential virological and immunological outcome of severe acute respiratory syndrome coronavirus infection in susceptible and resistant transgenic mice expressing human angiotensin-converting enzyme 2. J. Virol. *83*, 5451–5465. https://doi.org/10.1128/jvi.02272-08.

Yuan, S., Peng, L., Park, J.J., Hu, Y., Devarkar, S.C., Dong, M.B., Shen, Q., Wu, S., Chen, S., Lomakin, I.B., and Xiong, Y. (2020). Nonstructural protein 1 of SARS-CoV-2 is a potent pathogenicity factor redirecting host protein synthesis machinery toward viral RNA. Mol. Cell. *80*, 1055–1066.e6. https://doi.org/10.1016/j.molcel.2020.10.034.

Zhang, K., Miorin, L., Makio, T., Dehghan, I., Gao, S., Xie, Y., Zhong, H., Esparza, M., Kehrer, T., Kumar, A., et al. (2021). Nsp1 protein of SARS-CoV-2 disrupts the mRNA export machinery to inhibit host gene expression. Sci. Adv. *7*, eabe7386. https://doi.org/10.1126/sciadv.abe7386.

Züst, R., Cervantes-Barragán, L., Kuri, T., Blakqori, G., Weber, F., Ludewig, B., and Thiel, V. (2007). Coronavirus non-structural protein 1 is a major pathogenicity factor: implications for the rational design of coronavirus vaccines. PLoS Pathog. *3*, e109. https://doi.org/10.1371/journal.ppat.0030109.

STAR★METHODS

KEY RESOURCES TABLE

REAGENT or RESOURCE	SOURCE	IDENTIFIER
Antibodies		
Rabbit GAPDH	Cell Signaling Technology	Cat#2118S Lot#10; RRID: AB_561053
Mouse S6 Ribosomal Protein	Cell Signaling Technology	Cat#2317S Lot#4; RRID: AB_2238583
Rabbit SARS-CoV-2 Spike	Abcam	ab272504; RRID: AB_2847845
Rabbit SARS-CoV-1 nsp1 PAb	Narayanan et al. (2015)	N/A
Rabbit SARS-CoV N PAb	Harcourt et al. (2020)	N/A
Goat anti rabbit IgG Alexa Fluor 488	Invitrogen	A-11034
HRP-linked anti-rabbit IgG	Cell Signaling Technology	7074; RRID: AB_2099233
IRDye® 800CW Goat anti-Rabbit IgG Secondary Antibody	Li-cor	926-32,211
IRDye® 680RD Goat anti-Mouse IgG Secondary Antibody	Li-cor	926-68,070
Bacterial and virus strains		
SARS-CoV-2	World Reference Center of Emerging Viruses and Arboviruses [WRCEVA] at the University of Texas Medical Branch	SARS-CoV-2/human/USA/WA-CDC-WA1/2020 (WA1)
mutant SARS-CoV-2 (CoV2-mut)	This paper	N/A
Chemicals, peptides, and recombinant proteins		
Sodium pyruvate	Biological Industries	03-042-1B
Pen-strep solution	Biological Industries	03-031-1B
L-glutamine	Biological Industries	03-020-1B
Penicillin-Streptomycin-Nystatin Solution	Biological Industries	03-032-1B
TPCK trypsin	Thermo Scientific	20,233
Trypsin EDTA Solution A	Biological Industries	03-050-1B
TransIT®-LT1 Transfection Reagent	Mirus	MIR 2300
Tri-reagent	Sigma-Aldrich	T9429
Tragacanth	Sigma-Aldrich	G1128
SlowFade™ Gold Antifade Mountant	Invitrogen	S36936
Turbo DNase	Ambion	am2238
FastAP Thermosensitive Alkaline Phosphatase	Thermo Scientific	EF0651
T4 Polynucleotide Kinase	NEB	M0201
SuperScript III Reverse Transcriptase	Invitrogen	18,080,093
Cycloheximide	Sigma Aldrich	C7698
DTT	Bio Basic	DB0058
SUPERase•In™ RNase Inhibitor	Invitrogen	AM2696
Ruxolitinib	InvivoGen	tlrl-rux
Spermidine	Sigma Aldrich	85,558
4-Thiouridine (4sU)	Sigma Aldrich	T4509
Iodoacetamide	Sigma Aldrich	A3221
Strep-TactinXT DY-649	IBA-lifesciences	2-1568-050
Bolt™ 4 to 12%, Bis-Tris, 1.0 mm, Mini Protein Gels	Invitrogen	NW04120BOX
Precision Protein StrepTactin-HRP Conjugate	BioRad	1,610,381

(*Continued on next page*)

Continued

REAGENT or RESOURCE	SOURCE	IDENTIFIER
Mayer's Hematoxylin solution	Sigma Aldrich	MHS16
Apex Quick Dissolve LE Agarose	Genesee Scientific	20-102QD
Crystal violet	Sigma Aldrich	C6158
Methylcellulose solution	Sigma Aldrich	M0512
Crystal Violet solution (0.1%)	Biological Industries	01-986
Critical commercial assays		
Dual-Luciferase® Reporter Assay System	Promega	E1910
DIG luminescent detection kit	Roche	11,363,514,910
Dynabeads mRNA DIRECT Purification Kit	Invitrogen	61,012
Verikine Human IFN Beta ELISA Kit	pbl Assay Science	41,410
Click-iT™ Plus OPP Alexa Fluor™ 594 Protein Synthesis Assay Kit	Invitrogen	C10457
Direct-zol RNA Miniprep Kit	Zymo Research	R2050
qScript FLEX cDNA Synthesis Kit	Quanta Biosciences	95,049
Pierce™ BCA Protein Assay Kit	Thermo Scientific	23,225
ImmPRESS® HRP Horse Anti-Rabbit IgG PLUS Polymer Kit, Peroxidase	Vector Laboratories	MP-7801
Deposited data		
GEO	https://www.ncbi.nlm.nih.gov/geo/query/acc.cgi?acc=GSE200422	GSE200422
Mendeley	https://data.mendeley.com/drafts/jr96bw6m25	https://doi.org/10.17632/jr96bw6m25.1
Experimental models: Cell lines		
Calu-3	ATCC	HTB-55
Vero E6	ATCC	CRL-1586
HEK293T	ATCC	CRL-3216
VeroE6/TMPRSS2	Japanese Collection of Research Bioresources	JCRB1819
Experimental models: Organisms/strains		
Golden Syrian Hamsters (females; 4-5 weeks old)	Envigo	8903F
Oligonucleotides		
nsp1-ΔRB_F - (GGGACAGATCCC TACAGCAGTGGCGTTACTCGCGAG)	Sigma Aldrich	N/A
nsp1-ΔRB_R - (AGTAACGCCACTGCT GTAGGGATCTGTCCCCAACTCGTC)	Sigma Aldrich	N/A
nsp1-CD_F - (CCCTTGTTCCCATT TGCTGCCAACAGCACCTTCCGAT ATGC)	Sigma Aldrich	N/A
nsp1-CD_R - (GAAGGTGCTGTTG GCAGCAAATGGGAACAAGGGC GCAGG)	Sigma Aldrich	N/A
Leader_nsp1_F - (CCAACTTTCG ATCTCTTGTAGATCTGTTCTC TAAACGAACATGGAGA GTCTTGTACCCGG)	Sigma Aldrich	N/A
Leader_nsp1_R - (GGGGGAGGT GCTACACATTGATCCTAGCAGA AGCACAGGCTTACTTTTC AAACTGCGGATGTGACC)	Sigma Aldrich	N/A
digoxigenin-labeled rLuc riboprobe	Kamitani et al. (2006)	N/A

(*Continued on next page*)

Continued

REAGENT or RESOURCE	SOURCE	IDENTIFIER
digoxigenin-labeled random-primed probe corresponding to nucleotides 28,999 to 29,573 of the SARS-CoV-2 genome	Xie et al. (2020)	N/A
GFP qPCR F - (TGACCCTGAAGTT CATCTGC)	Sigma Aldrich	N/A
GFP qPCR R - (GAAGTCGTGCTG CTTCATGT)	Sigma Aldrich	N/A
18S qPCR F - (CTCAACACGGGA AACCTCAC)	Sigma Aldrich	N/A
18S qPCR R - (CGCTCCACCAAC TAAGAACG)	Sigma Aldrich	N/A
Recombinant virus PCR primer 1 - (GAATTCGAGCTCGGTACCT CGCGAATGC)	IDT	N/A
Recombinant virus PCR primer 2 - (ATAAGGATCAGTGCC AAGCTCGTCGCC)	IDT	N/A
Recombinant virus PCR primer 3 - (CGACGAGCTTGGCACTGAT CCTTATAGCAGTGGTGTTACCC GTGAACTCATG)	IDT	N/A
Recombinant virus PCR primer 4 - (CTATGTTAGCGCTAGCA CGTGGAACC)	IDT	N/A
Recombinant DNA		
pCAGGS-nsp1-WT	This Paper	N/A
pCAGGS-nsp1-ΔRB	This Paper	N/A
pCAGGS-nsp1-CD	This Paper	N/A
pRL-EMCV-FL	Kamitani et al. (2009)	N/A
pLVX-EF1alpha-SARS-CoV-2-nsp1-2XStrep-IRES-Puro	Nevan Krogan	N/A
pLVX-EF1alpha-SARS-CoV-2-nsp1ΔRB-2XStrep-IRES-Puro	This paper	N/A
pLVX-EF1alpha-SARS-CoV-2-nsp1CD-2XStrep-IRES-Puro	This paper	N/A
CoV2leader-acGFP	Finkel et al. (2021a)	N/A
control5′UTR-acGFP	Finkel et al. (2021b)	N/A
Cov2leader-nsp1WT	This Paper	N/A
Cov2leader-nsp1ΔRB	This Paper	N/A
Cov2leader-nsp1-CD	This Paper	N/A
Software and algorithms		
Bowtie v.1.1.2	(Langmead, 2009)	http://bowtie-bio.sourceforge.net/manual.shtml
DESeq2 (R package)	Love et al. (2014)	https://github.com/mikelove/DESeq2
STAR 2.5.3a	Dobin et al. (2013)	N/A
GRAND-SLAM	Jürges et al. (2018)	N/A
R 4.1.0	N/A	https://www.r-project.org/
Python 3.7.0	N/A	https://www.python.org/
Adobe Illustrator	Adobe	2021
FlowJo	TreeStar	Version 10.8.0
Fiji/ImageJ	Schindelin (2012)	RRID: SCR_003070; URL: https://imagej.net/Fiji

RESOURCE AVAILABILITY

Lead contact

Further information and requests for resources and reagents may be directed to and will be fulfilled by the lead contact, Noam Stern-Ginossar (noam.stern-ginossar@weizmann.ac.il).

Materials availability

All unique plasmids generated in the current study are available from the lead contact upon request. The SARS-CoV-2 recombinant virus generated in this study is available from Shinji Makino under an MTA with The University of Texas Medical Branch.

Data and code availability

All next-generation sequencing data files and genes expression values were deposited and made publicly available in Gene Expression Omnibus (GEO). Original western blot images and microscopy data have been deposited at Mendelay and are publicly available. Accession numbers are listed in the key resources table.

This paper does not report original code

Any additional information required to reanalyze the data reported in this paper is available from the lead contact upon request.

EXPERIMENTAL MODEL AND SUBJECT DETAILS

Cells lines viruses

Calu3 cells (ATCC HTB-55) were cultured in 6-well or 10-cm plates with Dulbecco's Modified Eagle Medium (DMEM) supplemented with 10% fetal bovine serum (FBS), MEM non-essential amino acids (NEAA), 2 mM L-glutamine, 100 units per ml penicillin and 1% Na-pyruvate. African green monkey kidney clone E6 cells (Vero E6, ATCC CRL-1586) were grown in growth medium DMEM containing 10% FBS, MEM NEAA, 2 mM L-glutamine, 100 Units/mL penicillin, 0.1 mg/mL streptomycin, 12.5 Units/mL nystatin (P/S/N), all from Biological Industries, Israel]. Calu3 monolayers were washed once with MEM-Eagles medium (MEM) without FBS and infected with SARS-CoV-2 in the presence of 20 μg per ml TPCK trypsin (Thermo scientific). Plates were incubated for 1 h at 37°C to allow viral adsorption. Then, MEM medium supplemented with 2% FBS, was added to each well. Virus was propagated and titered on Vero E6 cells and sequenced prior to use. Handling and working with SARS-CoV-2 were conducted in a BSL3 facility in accordance with the biosafety guidelines of the Israel Institute for Biological Research (IIBR), or in a BSL3 facility at The University of Texas Medical Branch (UTMB). The Institutional Biosafety Committee of Weizmann Institute and that of UTMB approved the protocol used in these studies. Calu3, Vero E6, and 293T cells were authenticated by ATCC using STR profiling. All cell lines tested negative for mycoplasma.

Animal study

All hamster experiments with virus infection were performed under biosafety level-3 agriculture (BSL-3 Ag) containment at the University of Wisconsin-Madison in laboratory space approved by the Centers for Disease Control and Prevention and by the US Department of Agriculture.The study included female Golden Syrian Hamsters aged 4-5 weeks old (Envigo 8903F).

METHOD DETAILS

Generation of recombinant infectious SARS-CoV-2

To generate CoV-2-mut, carrying a deletion of the amino acids 155 to 165 in the nsp1 gene of SARS-CoV-2 genome, a recombinant PCR procedure was employed to generate the deletion in fragment 1 of the SARS-CoV-2 reverse genetics system (Xie et al., 2020). The SARS-CoV-2 full-length cDNA was assembled from fragments 1 through 7 and used as the template for synthesizing the full-length RNA transcripts as described previously (Xie et al., 2020). The recombinant infectious viruses, CoV-2-wt and CoV-2-mut, were recovered using the full-length RNA transcripts, according to established protocols, as described previously (Xie et al., 2020).

Plasmid construction

SARS-CoV-2 nsp1 ORF, carrying a C-terminal myc-tag, was cloned into pCAGGS-MCS, resulting in pCAGGS-nsp1-WT. Similarly, SARS-CoV-2 nsp1 carrying a deletion of the amino acids 155 to 165, and SARS-CoV-2 nsp1 carrying R124A and K125A mutations, were cloned into pCAGGS to generate pCAGGS-nsp1-ΔRB and pCAGGS-nsp1-CD, respectively. The plasmid pRL-EMCV-FL, carrying an upstream, cap-dependent Renilla luciferase gene followed by an EMCV IRES-dependent firefly luciferase gene, was constructed, as described previously (Kamitani et al., 2009).

pLVX-EF1alpha-SARS-CoV-2-nsp1-2XStrep-IRES-Puro (nsp1-WT) was kindly provided by N. Krogan. The mutations to generate nsp1-ΔRB and nsp1-CD were introduced by amplifying the nsp1-WT plasmid so that it became a linear fragment containing the desired mutations (primers 1-4 listed in the key resources table).

For the reporter assay, reporter plasmids containing both the CoV-2 sub-genomic leader and a human control 5′UTR were used as described in(Finkel et al., 2021a). In order to express Nsp1-WT, nsp1-ΔRB, and nsp1-CD under the SARS-CoV-2 leader, the nsp1

cassette, including the twin strep II tag at the C-terminus of the protein, was lifted from their respective plasmids and inserted immediately downstream of the SARS-CoV-2 subgenomic leader sequence on the plasmid used in the reporter assay in place of the GFP cassette, using restriction-free cloning (primers 5 & 6 listed in the key resources table).

Virus infection and quantification

Recombinant wild-type SARS-CoV-2 (CoV-2-wt) and mutant SARS-CoV-2 (CoV-2-mut), both of which were rescued by using the reverse genetics system (Xie et al., 2020), were passaged once in Vero E6 cells, and used for infection studies. For virus growth analysis, Vero E6 and Calu3 cells were infected at the indicated m.o.i. for 1 h at 37°C. After virus adsorption, cells were washed twice and incubated with the appropriate medium. Culture supernatants were collected at the indicated times post-infection and the infectious virus titers were determined by plaque assay on Vero E6 cells, as described previously (Harcourt et al., 2020).

Luciferase assay

Vero E6 cells in 24-well plates were co-transfected, in triplicate, with pRL-EMCV-FL reporter plasmid and the indicated pCAGGS-based nsp1 expression plasmids using TransIT-LT1 reagent (Mirus). At 24 h post-transfection, the cells were lysed in Passive Lysis Buffer (Promega), and luciferase assays were performed using the Promega Dual Luciferase assay system.

Viral titers

For determination of growth kinetics of CoV2-wt or CoV2-mut, Vero E6 and Calu3 cells were seeded in 12-well plates. Twenty four h later, Calu3 cells were washed once with MEM supplemented with NEAA, glutamine, and P/S/N without FBS. Then, Calu3 and Vero E6 cells were infected at an MOI of 0.1 of CoV-2 wt or CoV-2 mut in infection medium (MEM containing 2% FBS with NEAA, glutamine, and P/S/N). For Calu3 cells, the infection medium was supplemented with 20 μg/mL TPCK trypsin (Thermo scientific). Plates were incubated for 1 h at 37°C to allow viral adsorption. Then, the infection medium was aspirated, the wells were washed once with infection medium and then MEM medium supplemented with 2% FBS and 0.15% sodium bicarbonate, was added. Culture media was collected at several time points: 0 h, 11 h, 24 h and 48 h. Cell debris were removed by centrifugation. The supernatants were kept for viral titer determination and the cell pellets were harvested by Tri-reagent (Merck, Israel) for RNA purification.

For viral titration, Vero E6 cells were seeded in 12-well plates and grown overnight in growth medium. Serial dilutions of each supernatant from each of the above indicated time points were prepared in infection medium and used to infect Vero E6 monolayers (200 μL/well). Plates were incubated for 1 h at 37°C to allow viral adsorption. Then, 2 mL/well of overlay [MEM containing 2% FBS and 0.4% tragacanth (Merck, Israel)] was added to each well and plates were incubated at 37°C, 5% CO_2 for 72 h. The media were then aspirated, and the cells were fixed and stained with 1 mL/well of crystal violet solution (Biological Industries, Israel). The number of plaques in each well was determined, and virus titers were calculated.

Experimental infection of syrian hamsters

Golden Syrian hamsters (females; 4-5 weeks old) were intranasally infected with 1000 PFU of virus in 50 μL of inoculum while under isoflurane anesthesia. Animals were checked daily to evaluate the health of the hamsters, including body weight. Three days and seven days after infection, tissues were collected after the animals were humanely euthanized.

Virus titers in the tissues were determined on confluent Vero E6/TMPRSS2 cells obtained from the Japanese Collection of Research Bioresources (JCRB) Cell Bank (1819). Cells were infected with 100 μL of undiluted or 10-fold dilutions (10^{-1} to 10^{-5}) of clarified lung and nasal turbinate homogenates for 30 min. After the inoculum was removed, the cells were washed once, and then overlaid with 1% methylcellulose solution in DMEM with 5% FBS. The plates were incubated for three days, and then the cells were fixed and stained with 20% methanol and crystal violet in order to count the plaques.

Immunohistochemistry staining for hamster tissues

Virally infected cells within the lungs were detected as described before (Tseng et al., 2007; Yoshikawa et al., 2009). Briefly, paraffin-embedded sections were firstly subjected to immunostaining with a commercially available and diluted (1:5,000) rabbit-anti-SARS-CoV-2 spike (S) protein (ab272504, Abcam Plc., Cambridge, UK), followed by staining with a peroxidase-conjugated secondary antibody. Thoroughly washed tissues were then incubated with a solution containing 3,3′-Diaminobenzidine as the substrates to visualize virally infected cells, according to the procedure recommended by the vendor (MP-7801, Vector Laboratories, Burlingame, CA). Finally, stained slides were counterstained with hematoxylin and antigen expression was examined under an inverted microscopy at different magnifications.

Immunofluorescence analysis

Vero E6 cells were either uninfected or infected with CoV2-wt or CoV2-mut at an MOI of 2. At 16 h p.i, cells were fixed with 4% paraformaldehyde in PBS overnight at 4°C and permeabilized with 0.1% Triton X-100 for 15 min at room temperature. Subsequently, the cells were subjected to immunofluorescence analysis using the anti-SARS-CoV-1 nsp1 antibody or an affinity-purified rabbit anti-SARS-CoV N polyclonal antibody (Harcourt et al., 2020) as primary antibodies, followed by Alexa Fluor 488-conjugated secondary antibody (Invitrogen) and DAPI counterstaining, using SlowFade Gold antifade reagent (Invitrogen). The cells were examined using an Olympus BX53 microscope with a 40X objective lens at UTMB and processed with ImageJ (NIH) software. For Figure S5A, cells were

plated on ibidi slides, infected as described in 'Cells and viruses' at an MOI of 3 or left uninfected and at 8hpi washed once with PBS, fixed in 3% paraformaldehyde for 20 min, washed in PBS, permeabilized with 0.5% Triton X-100 in PBS for 2 min, and then blocked with 2% FBS in PBS for 30 min. Immunostaining was performed with rabbit anti-SARS-CoV-2 serum (Yahalom-Ronen et al., 2020) at a 1:200 dilution. Cells were washed and labeled with anti-rabbit FITC conjugated antibodies at a 1:200 dilution and with DAPI (4′,6-diamidino-2-phenylindole) at a 1:200 dilution. Imaging was performed on a Zeiss AxioObserver Z1 wide-field microscope using a ×40 objective and Axiocam 506 mono camera.

Northern blot analysis

Northern blot analysis was performed using total intracellular RNAs, as described previously (Kamitani et al., 2006). A digoxigenin (DIG)-labeled rLuc riboprobe was used to detect the Renilla luciferase gene, as described previously (Kamitani et al., 2006). A DIG-labeled random-primed probe, corresponding to nucleotides 28,999 to 29,573 of the SARS-CoV-2 genome (Kamitani et al., 2006; Xie et al., 2020), was used to detect SARS-CoV-2 mRNAs and visualized by DIG luminescent detection kit (Roche, Indianapolis, IN), according to the manufacturer's protocol.

Preparation of RNA-seq samples

Virus-infected cells were collected at 4 and 7 hpi. For RNA-seq, cells were washed with PBS and then collected with Tri-Reagent (Sigma-Aldrich). Total RNA was extracted and poly-A selection was performed using Dynabeads mRNA DIRECT Purification Kit (Invitrogen). The mRNA sample was subjected to DNase I treatment and 3′ dephosphorylation using FastAP Thermosensitive Alkaline Phosphatase (Thermo Scientific) and T4 polynucleotide kinase (New England Biolabs) followed by 3′ adaptor ligation using T4 ligase (New England Biolabs). The ligated products were used for reverse transcription with SSIII (Invitrogen) for first-strand cDNA synthesis. The cDNA products were 3′-ligated with a second adaptor using T4 ligase and amplified for 8 cycles in a PCR for final library products of 200–300 bp.

Preparation of ribosome profiling samples

For ribosome profiling libraries, cells were treated with 100 μg/mL cycloheximide for 1 min. Cells were then placed on ice, washed twice with PBS containing 100 μg/mL cycloheximide, scraped from 10-cm plates, pelleted and lysed with lysis buffer (1% Triton in 20 mM Tris-HCl 7.5, 150 mM NaCl, 5 mM $MgCl_2$, 1 mM dithiothreitol supplemented with 10 U/mL Turbo DNase and 100 μg/mL cycloheximide). After lysis, samples stood on ice for 2 h and subsequent ribosome profiling library generation was performed, as previously described(Finkel et al., 2020). In brief, cell lysate was treated with RNase I for 45 min at room temperature followed by SUPERase-In quenching. Sample was loaded on sucrose solution (34% sucrose, 20 mM Tris-HCl pH 7.5, 150 mM NaCl, 5 mM $MgCl_2$, 1 mM dithiothreitol and 100 μg/mL cycloheximide) and spun for 1 h at 100,000 rpm using TLA-110 rotor (Beckman) at 4°C. The pellet was collected using TRI reagent and the RNA was collected using chloroform phase separation. For size selection, 10 μg of total RNA was loaded into 15% TBE-UREA gel for 65 min, and 28–34-nt footprints were excised using 28-nt and 34-nt flanking RNA oligonucleotides, followed by RNA extraction and ribosome profiling library construction as previously described.

Ruxolitinib assay

Calu3 cells were infected as described above with 0.1 MOI of CoV2-wt or CoV2-mut. After 1 h at 37°C, the cells were washed as detailed above and treated with 4 μM Ruxolitinib (InvivoGen). Fresh Ruxolitinib was added at 24hpi.

IFNβ ELISA assay

Calu3 cells were infected with CoV2-wt or CoV2-mut at an MOI of 0.1. Media was collected at 0, 24, and 48 h post infection, and IFNβ concentrations were measured using the Verikine Human IFN Beta ELISA Kit (pbl Assay Science) as per manufacturer instructions.

Protein synthesis measurement using OPP

The OPP assay (OPP, Thermo Fisher Scientific) was carried out following the manufacturer's instructions. In brief, cells were collected following treatment with 10 μM OPP for 30 min at 37°C. The cells were then fixed for 15 min in 3.7% formaldehyde, and permeabilized in 0.1% Triton X-100 for 15 min. OPP was then fluorescently labeled by a 30-min incubation in Click-iT Plus OPP reaction cocktail with Alexa Fluor 594 picolyl azide (Thermo Fisher Scientific). Cells were analyzed using BD LSRII flow cytometer. The decrease in translation levels was calculated according to the median Alexa 594 fluorescence intensity between the 7 hpi and uninfected samples.

Subcellular fractionation

293T cells transfected with a plasmid expressing Nsp1-WT, nsp1-ΔRB, nsp1-CD, or GFP were washed in PBS at 24 h post-transfection, trypsinized and resuspended in cold PBS. A fraction containing 10% of the cells was then transferred to a new tube and RNA was extracted in Tri-reagent to obtain whole cellular extract. Remaining cells were pelleted for 5 min at 300g. Cells were resuspended in 150 μL fractionation buffer A (15 mM Tris-HCl pH 8.0, 15 mM NaCl, 60 mM KCl, 1 mM EDTA pH 8.0, 0.5 mM EGTA pH 8.0, 0.5 mM spermidine, and 10 U ml^{-1} RNase inhibitor), and 150 μL 2x lysis buffer (15 mM Tris-HCl pH 8.0, 15 mM NaCl, 60 mM KCl, 1 mM EDTA pH 8.0, 0.5 mM EGTA pH 8.0, 0.5 mM spermidine,10 U/ml RNase inhibitor and 0.5% NP-40) was added followed by

10 min incubation on ice. The extract was pelleted for 5 min at 400g and the supernatant containing the cytoplasmic fraction was removed to a new tube. This was centrifuged again at 500g for 1 min, the supernatant was transferred to a new tube and RNA was extracted with Tri-reagent. The nuclear pellet was resuspended in 1 mL RLN buffer (50 mM Tris-HCl pH 8.0, 140 mM NaCl, 1.5 mM $MgCl_2$, 0.5% NP-40, 10 mM EDTA and 10 U/mL RNase inhibitor) and incubated on ice for 5 min. The nuclear fraction was then pelleted for 5 min at 500g, the supernatant was removed and RNA was extracted from the pellet with Tri-reagent. RNA-seq libraries were then prepared from all three fractions as described above.

RNA labeling for SLAM-seq

For metabolic RNA labeling of 293T cells transfected with a plasmid or infected Calu3 cells, growth medium was replaced with medium containing 4sU (T4509, Sigma) 24 h post-transfection or 3 hpi at a final concentration of 200 μM (a concentration that did not induce substantial cell cytotoxicity at 3 h labeling). Cells were collected with Tri-reagent at 2, 3, or 4 h after labeling for transfected cells or at 1, 2, or 3 h after labeling for infected cells (corresponding to 4, 5, and 6 hpi). RNA was extracted under reducing conditions and treated with iodoacetamide (A3221, Sigma) as previously described(Herzog et al., 2017). RNA-seq libraries were prepared and sequenced as described above.

Reporter assay

293T cells were transfected using JetPEI (Polyplus-transfection) following the manufacturer's instructions. Twenty-four h after transfection, cells were assayed for reporter expression by flow cytometry on a BD Accuri C6 flow cytometer. In parallel, cells were assayed for expression of nsp1 and reporter mRNA levels as detailed below.

Flow cytometry analysis of strep tag

The expression of nsp1 was verified by staining of the fused strep-tag, followed by flow cytometry. Cells were fixed in 4% paraformaldehyde, permeabilized in 0.1% Triton X-100, and stained using Strep-TactinXT DY-649 (IBA-lifesciences). Flow cytometry analysis was performed on BD Accuri C6 and analyzed on FlowJo. Normalization to the mode is presented in the histograms.

Quantitative real-time PCR analysis

Total RNA was extracted using Direct-zol RNA Miniprep Kit (Zymo Research) following the manufacturer's instructions. cDNA was prepared using qScript FLEX cDNA Synthesis Kit with random primers (Quanta Biosciences) following the manufacturer's instructions.

Real-time PCR was performed using the SYBR Green PCR master-mix (ABI) on the QuantStudio 12K Flex (ABI) with the following primers (forward, reverse): GFP (TGACCCTGAAGTTCATCTGC, GAAGTCGTGCTGCTTCATGT); and 18S (CTCAACACGGGAAAC CTCAC, CGCTCCACCAACTAAGAACG).

GFP mRNA levels were calculated relative to 18S rRNA. Three technical replicates of one representative experiment of two total experiments are shown (Figures 1D and 1F).

Ribosome pelleting and western blot analysis

293T cells were transfected with nsp1-WT, nsp1-ΔRB, or nsp1-CD. At 24 h post-transfection cells were lysed in lysis buffer (1% Triton in 20 mM Tris-HCl, pH 7.5, 150 mM NaCl, 5 mM $MgCl_2$, 1 mM dithiothreitol and 10 U/ml Turbo DNase). The lysate was loaded on sucrose solution (34% sucrose, 20 mM Tris-HCl, pH 7.5, 150 mM NaCl, 5 mM $MgCl_2$, and 1 mM dithiothreitol) and spun for 1 h at 100,000 rpm using TLA-110 rotor (Beckman) at 4°C. The ribosome pellet was suspended in RIPA buffer (150mM sodium chloride, 1X Triton X-100, 0.5% sodium deoxycholate, 50mM Tris pH8.0, 0.1X SDS, and Complete protease inhibitor (1 tablet or 1 mL of 10x prot. inh.)), and the amount of protein was quantified from both the ribosomal fraction as well as the whole lysate by Pierce BCA Protein Assay (Thermo Fisher Scientific). Samples were then separated by 4-12% polyacrylamide Bis-tris gel electrophoresis (Invitrogen), blotted onto a nitrocellulose membrane and immunoblotted with Streptactin-HRP (Bio-rad), αRPS6 (Cell signaling Technology, 2317), and αGAPDH (Cell signaling Technology, 2118). Secondary antibodies used were goat anti-rabbit or goat anti-mouse (IRDye 800CW or IRDye 680RD, Li-Cor). Reactive bands were detected by Odyssey CLx infrared imaging system (Li-Cor) and quantified using Fiji (ImageJ) as detailed in https://imagej.nih.gov/nih-image/manual/tech.html. For Figure 3, Western blot analysis was performed, as described previously (Kamitani et al., 2006). An affinity-purified rabbit anti-SARS-CoV-1 nsp1 polyclonal antibody (Narayanan et al., 2015) was used as the primary antibody, and an HRP-linked anti-rabbit IgG (Cell Signaling Technology) was used as the secondary antibody.

Graphics

Figures 1A, S8, and S2C were created using BioRender. Fluorescence-activated cell sorting figures were created with FlowJo and the rest of the figures were drawn with ggplot2 in R.

QUANTIFICATION AND STATISTICAL ANALYSIS

Sequence alignment and metagene analysis

Sequencing reads were aligned as previously described(Finkel et al., 2021b). In brief, linker (CTGTAGGCACCATCAAT for FP libraries and AGATCGGAAGAGCACACGT for mRNA libraries) and poly-A sequences were removed. Next, reads were aligned to a reference containing human rRNA and tRNA, and all reads that were successfully aligned were filtered out, and the remaining reads were aligned to the hg19 and to the SARS-CoV-2 genome (Genebank NC_045,512.2). Alignment was performed using Bowtie v.1.1.229 with a maximum of two mismatches per read. Reads that were not aligned to the genome were aligned to the transcriptome (using the known canonical isoform UCSC gene annotations) and to SARS-CoV-2 junctions that were recently annotated(Kim et al., 2020). The aligned position on the genome was determined as the 5′ position of RNA-seq reads, and for ribosome profiling reads the p-site of the ribosome was calculated according to read length using the offset from the 5′ end of the reads that was calculated from canonical cellular open reading frames. The offsets used were +12 for reads that were 28 or 29 bp and +13 for reads that were 30–33 bp. Footprint reads that were of other lengths were discarded. For the metagene analysis only genes with CDS length of at least 300 nucleotides, UTRs of at least 50 nucleotides and more than 50 reads in the analyzed window around the start or the stop codon were used. For each gene, reads were normalized to the position with the maximal number of reads in that gene, and then averaged.

Differential gene expression analysis

Differential expression analysis was done using DESeq2 (Love et al., 2014). ISG enrichment was calculated using a hypergeometric test, using a p value threshold of 0.001.

Gene filtering, quantification and normalization

RNA-seq read coverage on CDS was normalized to Reads Per Kilobase of transcript, per Million mapped reads (RPKM) to normalize for CDS length and sequencing depth. For analysis in which host and viral gene expression were compared (Figure 4 and S7), RPKM was normalized based on the number of reads uniquely aligned to the coding regions of both the host and the virus. For analysis that was focused on cellular gene expression, the RPKM was normalized based on the number of reads aligned to the rRNA and tRNA. This number was estimated by using the ratio of rRNA and tRNA reads to cellular aligned reads in a total RNA sequencing (without polyA selection). For footprint libraries, read coverage of cellular and viral genes was normalized to RPKM based on the number of reads aligned uniquely to the host total CDS aligned ribosome profiling host reads. Because the viral subgenomic transcripts are widely overlapping, RNA-seq RPKM levels of viral genes were computed with deconvolution as was previously described (Irigoyen et al., 2016; Kim et al., 2020). First, from the RPKM values of each subgenomic transcript, the RPKM of the upstream subgenomic (or the RPKM of ORF1b for the first subgenomic) transcript was subtracted. Then, for subgenomic transcripts, leader–body junctions were quantified on the basis of the number of uniquely mapped reads that span each canonical junction using STAR 2.5.3a aligner(Dobin et al., 2013). Finally, on the basis of the correlation between the deconvoluted RPKM and junction abundance of the subgenomic RNAs, the RPKM levels of all viral RNAs (including the genomic RNA) were estimated. Viral and host gene translation efficiency was calculated as the ratio between footprint RPKM and RNA-Seq RPKM. For cellular gene quantification, the number of reads aligned to the CDS of each gene in each replicate had to be greater than 10 reads.

Quantification of intronic reads

To avoid biases from intron read count, first reads which are aligned to exons were excluded. Then the counting of reads for the introns was as described above for the exons, with intron annotations based on the known canonical isoform UCSC gene annotations. In addition, genes with a low number of reads (<10 on the exons and <2 on the introns) were omitted. The number of reads on exons and introns was normalized by the total length of the exons and introns, respectively, to get a quantification proportional to the number of molecules. Finally, the normalized number of reads on introns was calculated as a percentage of the normalized number of reads on exons. Genes with an intronic to exonic ratio of >1 were excluded from the analysis. Statistical significance (Figure 5H) was tested using a paired t test on the log values of the percentage.

Subcellular fractionation analysis

RNA-seq reads from total, nuclear and cytosolic fractions were aligned to the human and viral reference as described above. Human gene read counts were adjusted to RPKM as described above, and then converted to transcripts per million (TPM) by normalizing to the sum of RPKM in each sample, so that the expression levels in each sample sum up to the same value.

A list of 2203 average-expressed genes was defined. These genes were genes with 15 or more reads across all samples and with a sum of TPM values in the total RNA samples across replicates within quantiles 0.4 and 0.9. On the basis of this list, for each replicate, a linear regression model was calculated of the total fraction as a linear combination of the cytosolic and the nuclear fractions. The regression coefficients were used to normalize the cytosolic and nuclear TPM values to obtain absolute localization values(Carlevaro-Fita et al., 2019). To correct for changes in total mRNA levels, the absolute values were further scaled by a factor calculated from total RNA-seq as described in ‘Gene filtering, quantification and RPKM normalization. To statistically compare the effect of infection on nuclear–cytosolic distribution of mRNAs from different clusters, p values were calculated from the interaction term in a linear model.

SLAM-seq analysis and half-life calculation

Alignment of SLAM-seq reads was performed using STAR(Dobin et al., 2013; Herzog et al., 2017), with parameters that were previously described(Finkel et al., 2021b). First, reads were aligned to a reference containing human rRNA and tRNA, and all reads that were successfully aligned were filtered out. The remaining reads were aligned to a reference of the human and the virus as described above. Reads mapped to the virus were discarded and reads mapped to the human were used in the next steps. Output.bam files from STAR were used as input for the GRAND-SLAM analysis(Jürges et al., 2018) with default parameters and with trimming of 5 nucleotides in the 5′ and -3′′ends of each read. Infected and uninfected samples were analyzed in separate runs. Each one of the runs also included an unlabeled sample (no 4sU) that was used for estimating the linear model of the background mutations. The output of GRAND-SLAM, i.e., the estimated ratio of newly synthesized out of total molecules for each gene (new to total ratio (NTR)), was used to calculate the half-life as described below. The old transcript fraction for each gene in each sample is 1 – NTR; this number reflects the pre-existing mRNA molecules (not labeled) and these values were used for half-life estimation of cellular genes. The half-life of each gene was calculated by linear regression of the log values of the calculated old transcript fraction. Estimated variance of the values as calculated by GRAND-SLAM were used as weights in the linear regression. The regression coefficient λ was converted to half-life as $-\log(2)/\lambda$. For further analysis, only genes for which the p value in the regression was <0.1 and the adjusted r2 > 0.7 were used.